RESEARCH ARTICLE | FEBRUARY 09 2026

Impact of gas carrier on inhaled medicinal aerosolized particles transport and deposition in a human respiratory system: A computational fluid particle dynamics study FREE

Hang Yi ; Yu Feng

Physics of Fluids 38, 021908 (2026)
https://doi.org/10.1063/5.0310825

Physics of Fluids ARTICLE pubs.aip.org/aip/pof

Impact of gas carrier on inhaled medicinal aerosolized particles transport and deposition in a human respiratory system: A computational fluid particle dynamics study

Cite as: Phys. Fluids **38**, 021908 (2026); doi: 10.1063/5.0310825
Submitted: 5 November 2025 · Accepted: 22 January 2026 ·
Published Online: 9 February 2026

Hang Yi and Yu Feng[a)]

AFFILIATIONS

School of Chemical Engineering, Oklahoma State University, 420 Engineering North, Stillwater, Oklahoma 74078, USA

[a)]Author to whom correspondence should be addressed: yu.feng@okstate.edu

ABSTRACT

This study investigated how the hydrogen–oxygen (H_2–O_2) gas mixture (2:1 by volume) as an alternative particle carrier could enhance aerosolized medicinal delivery efficiency to the peripheral lung (i.e., generation 13-to-alveoli region) compared with air. Employing an experimentally validated computational fluid particle dynamics model, this paper predicted and compared pulmonary air-particle vs H_2–O_2-particle transport and deposition in a representative human respiratory system, using multiple particle sizes (i.e., 1, 5, and 10 μm) and breathing patterns (12, 16, and 20 breaths per min with a fixed tidal volume of 500 ml). Results show that using the H_2–O_2 gas mixture rather than air produces lower Reynolds numbers, reducing turbulence intensity and flow resistance in the respiratory system under all three breathing patterns investigated in this study. It also creates a milder mechanical ventilation environment with lower wall shear stress, thereby minimizing airway irritation. Accordingly, inertial impaction and turbulence-driven deposition in the upper airways decreased, allowing more particles to reach the peripheral lung. Across all cases, the H_2–O_2 mixture allows more particles to reach the peripheral lung, improving delivered efficiency by up to 9.16%. Simulations further reveal that slower breathing (i.e., lower breathing frequency) and smaller particle size (i.e., 1 μm) can further enhance particle delivery efficiency to the peripheral lung. The findings mentioned above confirm the potential of the H_2–O_2 gas mixture as carrier to enhance drug delivery to small airways via inhalation therapy compared with air alone. Nevertheless, before clinical translation, potential adverse health effects, such as risks of hyperoxia, require further *in vivo* evaluation.

I. INTRODUCTION

As one of the most widely used treatments for respiratory disorders such as asthma, chronic obstructive pulmonary disease (COPD), cystic fibrosis, and pulmonary infections, inhalation therapy delivers medication directly through pulmonary routes, enhancing therapeutic effect by bypassing systemic circulation compared to systemic administration routes such as oral injection and intravenous injection (Borghardt *et al.*, 2018). However, the efficiency of drug delivery to the small airways remains limited in conventional inhalation therapies, thereby constraining treatment effectiveness. To improve the effectiveness of inhalation therapy, previous efforts were mainly on correct device selection, proper patient techniques, and ongoing education from healthcare professionals (Steiropoulos *et al.*, 2021). Specifically, historical focuses from physicians, patients, and researchers mainly were on: (1) Choosing an appropriate inhaler [e.g., metered-dose inhalers (MDIs), dry powder inhalers (DPIs), or nebulizers], which highly depends on the individual's age, coordination, and cognitive abilities (Hagmeyer *et al.*, 2023); (2) training patients for optimal coordination with the inhalers to ensure the medication reaches small airways more effectively (Fung and Siu, 2019); (3) securing prime administration techniques by integrating proper timing of actuation and inhalation, controlled breathing patterns, and adherence to the treatment plan for good therapeutic outcomes (Scichilone, 2015; Takemura *et al.*, 2011); and (4) optimizing aerosolized particle sizes and injection location, and generally finding the optimal diameter range (e.g., 1–5 μm) can penetrate deep lung sites and avoid deposition in the upper airways (Newman *et al.*, 1982; van der Zwaan *et al.*, 2024).

Indeed, the strategies mentioned above enhanced the delivered dose to small airways, patient compliance, and disease management,

particularly in asthma, COPD, and other respiratory conditions. While the research community on aerosolized medicinal particle inhalation has dominated this field, the role of the drug carrier gas has often been overlooked. The composition of drug carrier gas can potentially vary the Reynolds number and flow regime, which will have a significant impact on particle transport and deposition in human respiratory systems, and has often been treated as a predetermined or secondary factor. For example, inhalation therapy typically uses ambient air as the transport medium, but the physical properties of the gas (i.e., density, viscosity, diffusivity, and thermal conductivity) strongly affect gas-particle pulmonary flow dynamics. Meanwhile, carrier gases can interact with the airway environment, such as humidity and temperature, modifying particle size change due to water vapor condensation and particle–particle agglomeration.

Specifically, under the hypothesis that lighter gases (e.g., helium–oxygen gas mixture or so-called heliox) could reduce resistance to airflow, potentially enabling deeper penetration of inhaled aerosols, researchers have been incorporating carrier gas optimization into inhaler design, which can provide a new pathway to enhance drug delivery efficiency, reduce side effects, and improve outcomes in inhalation therapy (Farooq *et al.*, 2025; 2023; Islam *et al.*, 2020; and Saha and Islam, 2021).

Beyond the research conducted using heliox, multiple comprehensive reviews of clinical studies also highlighted the potential benefits of using hydrogen–oxygen (H_2–O_2) gas mixture in treating respiratory diseases, through both physical (i.e., gas properties) and biological (i.e., anti-inflammatory) mechanisms (Johnsen *et al.*, 2023; Zajac *et al.*, 2025). Specifically, Zheng *et al.*(2021) conducted a robust multicenter, randomized, double-blind, controlled clinical trial by comparing H_2–O_2 gas mixture inhalation vs O_2 therapy in acute exacerbation of chronic obstructive pulmonary disease (AECOPD) patients. Patients receiving H_2–O_2 inhalation showed greater improvement in symptoms and experienced fewer adverse events, as measured by the breathlessness, cough, and sputum scale (BCSS), compared with those receiving O_2 alone. Guan *et al.* (2020) conducted a randomized controlled trial, which demonstrated that H_2–O_2 inhalation significantly eased disease severity and dyspnea in COVID-19 patients, likely due to the decreased airway resistance and improved inspiratory effort. Another study focusing on the Omicron variant found faster viral shedding, higher lymphocyte recovery, and reduced interleukin-6 (IL-6) levels in patients treated with the H_2–O_2 mixture compared with O_2 (Shi *et al.*, 2023). Involving 20 asthma and COPD patients who inhaled a 2.4% H_2-containing steam mixed gas for a single inhalation period of 45 min, Wang *et al.* (2020) examined the acute effects of inhalation of H_2-containing gas and found that the treatment attenuated the inflammation status in asthma and COPD patients. Their results showed that this treatment can significantly decrease markers of inflammation, such as monocyte chemotactic protein 1, interleukin-4 (IL-4), and interleukin-6 (IL-6), in both COPD and asthma patients.

Prompted by clinical evidence demonstrating the anti-inflammatory benefits of H_2–O_2 therapy for lung diseases, the lightweight H_2–O_2 gas mixture shows excellent potential as a novel carrier gas for inhalation therapy superior to air. However, how this gas composition affects the transport and deposition of inhaled particles across varying particle sizes and breathing patterns remains understudied, particularly with respect to targeted delivery to small airways, a crucial step toward optimizing future inhaler therapies for COPD and asthma. To assess its potential compared to air, three key scientific questions must be addressed:

(1) Impaction of H_2–O_2 density on particle transport dynamics: According to Graham's law of diffusion and the Bernoulli principle, the lower density of the H_2–O_2 mixture allows a lower Reynolds number at the same inhalation volumetric flow rates, resulting in less turbulence. Therefore, whether using H_2–O_2 gas carrier can potentially reduce the turbulence dispersion-induced particle deposition in the upper airway and increase particle deposition in the small airways needs to be investigated.
(2) Therapeutic effect of H_2–O_2 gas mixture on a disease-specific level: Potentially, the reduced density can decrease inspiratory effort and the overall work of breathing in patients with compromised lung function, such as asthma or COPD (Zhou *et al.*, 2019), and the oxygen component alleviates hypoxemia, and the hydrogen provides antioxidant and anti-inflammatory effects beneficial for diseases like asthma and cystic fibrosis (Zhang *et al.*, 2018). Whether there will be additional therapeutic effects of H_2–O_2 gas mixture for other lung disease treatments should be further studied.
(3) Safety assessment of H_2–O_2 inhalation: Unlike O_2-rich, such as pure O_2 carriers that may induce hypercapnia in COPD patients, the H_2–O_2 gas mixture can potentially mitigate this risk, emphasizing the importance of tailoring gas compositions to patient conditions (Bardsley *et al.*, 2018; Jin *et al.*, 2025). Thus, quantifying the exposure risks with various H_2–O_2 compositions is necessary to identify the optimal H_2–O_2 gas mixture for inhalation therapy.

Focusing on addressing the first scientific question mentioned and enhancing fundamental understanding of how gas carriers can potentially enhance the targeted drug delivery to small airways for better therapeutic outcomes, this study employed an experimentally validated computational fluid particle dynamics (CFPD) framework for predicting gas-particle flow dynamics in human respiratory systems (Feng *et al.*, 2016; 2015; 2017; Haghnegahdar *et al.*, 2019). Indeed, CFPD (Bui *et al.*, 2020; Feng *et al.*, 2021; Kleinstreuer and Zhang, 2010; Kuprat *et al.*, 2025; and Tian and Ahmadi, 2021) has become a cornerstone of modern inhaled drug delivery research by enabling the prediction of spatiotemporal distributions of variables during the aerosol transport and deposition that are difficult to obtain through experimental studies alone (Longest *et al.*, 2019). Many existing publications have extensively demonstrated that CFPD holds the strong capability to facilitate inhalation therapy research community in conducting cutting-edge research topics, mainly by (1) advancing deposition prediction and device optimization including achieving pulmonary targeted delivery (Ainetdinov *et al.*, 2026) and optimizing inhaler design to reduce drug loss and evaluating smart inhalers and new strategies such as controlled condensational growth (Longest *et al.*, 2019); (2) addressing patient and disease variability such as modeling subject-specific airway anatomy to understand intersubject variability (Hofmann, 2011) and simulating drug delivery in constricted airways in asthma/COPD and for special populations like infants/children (Longest *et al.*, 2019); and (3) integrating with pharmacological models such as providing detailed deposition for physiologically based pharmacokinetic/pharmacodynamic

(PBPK/PD) models to predict drug absorption and systemic effects, supporting model-informed drug development (Feng *et al.*, 2021).

Indeed, understanding pulmonary gas-particle flow dynamics in human respiratory function is crucial for advancing pulmonary healthcare. The validated first-principle-based and high-fidelity CFPD model can quantify the spatiotemporal distributions of variables of interest in subject-specific human airways (e.g., gas flow velocity, pressure, turbulence kinetic energy (TKE), wall shear stress (WSS), and particle trajectories) in a cost-effective, noninvasive, and time-saving manner. It can overcome the inherent limitations of traditional *in vitro/in vivo* methods. In this study, CFPD simulations were carried out in a representative human respiratory system to investigate the drug particle transport and deposition patterns with different gas carriers (i.e., H_2–O_2 gas mixture with a volumetric ratio of 2:1 vs air), three transient breathing waveforms [i.e., breaths per min (BPM) = 12, 16, and 20 with a fixed tidal volume of 500 ml], and three particle diameters (i.e., 1, 5, and 10 μm), respectively. One-way coupled Euler–Lagrange model (Feng *et al.*, 2021) was employed to simulate gas-particle transport and deposition. The representative human respiratory system contains the respiratory tract from the mouth to generation 13 (G13) (Chen *et al.*, 2024). Quantitative CFPD results generated in this study help us have a better understanding of the potential of using H_2–O_2 gas mixture as particle carrier to enhance therapeutic efficiency to treat lung diseases.

II. METHODOLOGY

A. Geometry and mesh

As depicted in Fig. 1, a 3D subject-specific mouth-to-G13 airway geometry was developed based on existing research efforts by integrating a mouth-to-trachea upper airway (Banko *et al.*, 2016; Zhang *et al.*, 2012) from computed tomography (CT) scans of a male volunteer (47 yr old, 174 cm in height, 78 kg in weight, and no medical history of respiratory diseases) and an anatomically realistic tracheobronchial (TB) tree created using Lung4Cer based on a stochastic algorithm (Kitaoka *et al.*, 2013). It is worth noting that the mouth-to-G13 model has been employed in our previous publication (Chen *et al.*, 2024). A circular mouth opening with a diameter $D_{in} = 20$ mm was designed to replicate the hydraulic diameter of an inhaler mouthpiece. This representative respiratory system geometry comprises 375 individual airway structures and 188 distal terminal airways, with the most distal airways being G13. The smallest hydraulic diameter in the G13 openings is 1.02 mm, matching that of the preterminal bronchioles.

Using Ansys Fluent Meshing 2023 R1 (Ansys, Inc., Canonsburg, PA), a poly-hexcore meshing strategy was employed to generate the finite volume mesh. Five near-wall prism layers were generated to ensure $y^+ < 1$ for accurately capturing laminar-to-turbulence transition regions, where y^+ represents the dimensionless position of the first computational cell from the airway wall (Menter *et al.*, 2006). The final mesh employed in this study was generated using a similar meshing strategy as documented in existing publications (Feng *et al.*, 2017; 2018), which was also validated and employed in an existing publication (Chen *et al.*, 2024). The final mesh comprises 2 997 823 volume cells, 14 334 985 faces, and 9 136 173 nodes.

B. Governing equations

In this study, a one-way coupled Euler–Lagrange method (Benra *et al.*, 2011), namely, discrete phase model (DPM), was employed to investigate gas carrier influence on inhaled medicinal aerosolized particles transport and deposition. It is assumed the gas flow field

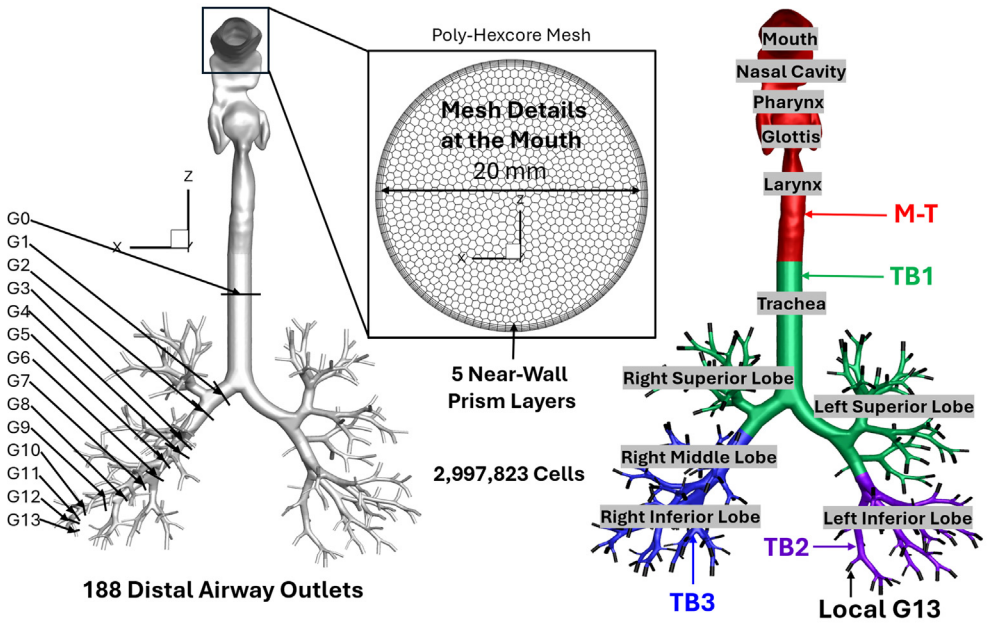

Abbreviations: (1) M-T: Mouth to Trachea, (2) TB: Tracheobronchial Tree, and (3) G0-G13: Generation 0 to Generation 13.

FIG. 1. Geometry and mesh details of the human respiratory system employed in this study.

influences the dilute particle suspension transport dynamics, while the dilute particle suspension does not influence the gas flow field.

1. Continuous phase (gas mixture)

For a continuous phase (i.e., H_2–O_2 gas mixture or air flow), an experimentally validated k–ω transition shear stress transport (SST) model (Chen *et al.*, 2017; Liu *et al.*, 2024; and Zhang and Kleinstreuer, 2011) was employed to predict laminar-to-turbulence transitional airflow characteristics through the airway over three complete breathing cycles with (1) the duration ratio between inhalation and exhalation equal to 1:2, (2) a fixed tidal volume of 500 ml, and (3) breathing frequencies equal to 12, 16, and 20 BPM. The breathing waveforms for three inhalation–exhalation cycles are shown in Fig. 2. The inhaled air is composed of 79% N_2 and 21% O_2, and the H_2–O_2 mixture consists of 2/3 H_2 and 1/3 O_2 (Liu *et al.*, 2025), respectively. The specific gas physical properties (Rocourt *et al.*, 2008) are shown in Table I. For binary gas species transport, the advection–diffusion equation for species A can be written as

$$\frac{\partial \rho Y_A}{\partial t} + \nabla \cdot (\rho \vec{u} Y_A) = \nabla \cdot (\rho D_{AB} \nabla Y_A), \tag{1}$$

where ρ is mixed gas density, $\vec{u}$ is the gas flow velocity, D_{AB} is the molecular diffusivity between gases in the continuous phase domain, and Y_A is the mass fraction of species A. Accordingly, the mass fraction of species B (Y_B) can be calculated by

$$Y_B = 1 - Y_A. \tag{2}$$

The continuity equation (total mass), momentum equation, and energy equation can be written as

$$\frac{\partial \rho}{\partial t} + \nabla \cdot (\rho \vec{u}) = 0, \tag{3}$$

$$\frac{\partial (\rho \vec{u})}{\partial t} + \nabla \cdot (\rho \vec{u} \vec{u}) = -\nabla p + \nabla \cdot \vec{\tau} + \rho \vec{g}, \tag{4}$$

$$\rho c_p \left(\frac{\partial T}{\partial t} + \vec{u} \cdot \nabla T \right) = \nabla \cdot (k_{eff} \nabla T) + \vec{\tau} : \nabla \vec{u} + \rho D_{AB} \sum\nolimits_{i=A \text{ or } B} c_{p,i} \nabla Y_i \cdot \nabla T, \tag{5}$$

in which p is pressure, $\vec{g}$ is the gravitational acceleration, $\vec{\tau} = \mu(\nabla \vec{u} + (\nabla \vec{u})^T)$ is the viscous stress tensor, μ is the dynamic viscosity, T represents temperature, k_{eff} is the effective thermal conductivity, which is the sum of thermal conductivity k, and turbulent thermal conductivity k_t, $c_{p,i}$ is the specific heat capacity of gas species A or B. It is worth noting that the Soret effect and thermophoresis are insignificant for the pulmonary gas flow field employed in this study. The quantitative evidence can be found in the supplementary material. To ensure the closure of the equation system, the ideal gas law was also employed, i.e.,

$$p = \frac{\rho \Re T}{M_{mix}}, \tag{6}$$

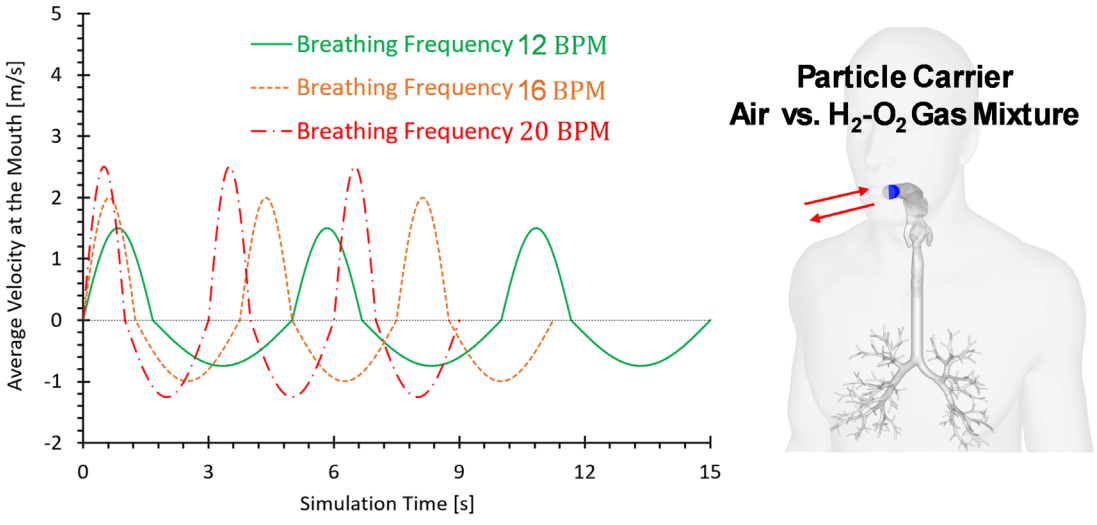

FIG. 2. Breathing waveforms employed in this study with different BPMs and a fixed tidal volume of 500 ml.

TABLE I. Physical properties of gases employed in this study.

	ρ_i (kg m^{-3})	$c_{p,i}$ (J kg^{-1} K^{-1})	k_i (W m^{-1} K^{-1})	μ_i (Pa s)	D_{AB} (m^2 s^{-1})
N_2	1.145	1.04×10^3	2.46×10^{-2}	1.78×10^{-5}	2.42×10^{-5} (N_2–O_2)
O_2	1.308	9.18×10^2	2.46×10^{-2}	2.05×10^{-5}	⋯
H_2	8.189×10^{-2}	1.428×10^4	1.672×10^{-1}	8.41×10^{-6}	7.77×10^{-5} (H_2–O_2)

where $\Re$ is the universal gas constant [8.314 J/(mol K)], and M_{mix} is the molar mass of the gas mixture, which can be calculated by

$$M_{mix} = \left(\sum_{i=A\ or\ B} \frac{Y_i}{M_i}\right)^{-1}. \tag{7}$$

Furthermore, the mixed gas properties ρ, c_p, and k can be calculated using the following equations:

$$\rho = \frac{pM_{mix}}{\Re T}, \tag{8}$$

$$c_p = \sum_{i=A\ or\ B} Y_i c_{p,i}(T), \tag{9}$$

$$k = \sum_{i=A\ or\ B} X_i k_i(T), \tag{10}$$

$$X_i = \frac{Y_i M_i}{\sum_{i=A\ or\ B} Y_i M_i}, \tag{11}$$

where M_i is the molecular mass of gas species i, X_i is the mole fraction of gas species i, and $k_i(T)$ is the thermal conductivity of gas species i.

2. Discrete phase (particles)

To investigate the particle size influence on particle transport and deposition, three different sizes of monodispersed and spherical injected particles at the mouth opening were considered (i.e., $d_p = 1$, 5, and 10 μm), respectively. In this study, the physical properties of the investigated aerosolized particles were assumed equivalent to physiological saline, with particle density $\rho_p = 1030\ \mathrm{kg/m^3}$. Particle trajectories were predicted by solving the particle translation equation (i.e., Newton's second law), where the drag force $\vec{F}_D$, thermophoretic force $\vec{F}_{TH}$, Saffman lift force $\vec{F}_L$, and gravity $\vec{F}_G$ as the primary forces (Lukerchenko *et al.*, 2012) act on particles. Brownian motion-induced force was neglected since it is insignificant for particles with an aerodynamic diameter equal to or larger than 1 μm (Heyder *et al.*, 1986). Specifically, the particle translation equation can be given as

$$m_p \frac{d\vec{u}_p}{dt} = \vec{F}_D + \vec{F}_{TH} + \vec{F}_L + \vec{F}_G, \tag{12}$$

where m_p and $\vec{u}_p$ represent the particle mass and velocity, respectively. $\vec{F}_D$ is given by

$$\vec{F}_D = \frac{1}{8}\pi\rho d_p^2 C_D(\vec{u} - \vec{u}_p)|\vec{u} - \vec{u}_p|/C_c, \tag{13}$$

where d_p denotes the particle diameter, C_c represents the Cunningham correction factor, and C_D refers to the drag coefficient (Chen *et al.*, 2018), given by

$$C_D = a_1 + \frac{a_2}{Re_p} + \frac{a_3}{Re_p}. \tag{14}$$

The constants a_1, a_2, and a_3 can be determined based on the particle Reynolds number, Re_p, which was defined as (Morsi and Alexander, 1972)

$$Re_p = \frac{\rho|\vec{u} - \vec{u}_p|d_p}{\mu}. \tag{15}$$

The Cunningham correction factor C_c was given by (Allen and Raabe, 1985)

$$C_c = 1 + \frac{2\lambda}{d_p}\left(1.257 + 0.4e^{-0.55\frac{d_p}{\lambda}}\right), \tag{16}$$

in which λ is the mean free path of air or H_2–O_2 gas mixture.

Considering the existing temperature gradient ∇T in the gas from the mouth under the ambient temperature to the airways under normal body temperature, this work took the thermophoretic force $\vec{F}_{TH}$ (i.e., Ludwig–Soret effect) into consideration, which drives particles suspended in the fluid domain (Derjaguin., 1976; Mason and Chapman, 1962; and Walker *et al.*, 1980). For spherical particles transporting in the ideal fluid domain, $\vec{F}_{TH}$ calculated by (Talbot *et al.*, 1980)

$$\vec{F}_{TH} = -K_{TH}\frac{\nabla T}{T_\infty}, \tag{17}$$

$$K_{TH} = \frac{6\pi d_p \mu^2 C_s(K + C_t K_n)}{\rho(1 + 3C_m K_n)(1 + 2K + 2C_t K_n)}, \tag{18}$$

$$\mu = \sum_{i=A\ or\ B} X_i \mu_i(T), \tag{19}$$

$$K = \frac{15\mu d_p}{8k_p}, \tag{20}$$

$$K_n = \frac{2\lambda}{d_p}, \tag{21}$$

where μ is gas dynamic viscosity. K_{TH} is the thermophoretic coefficient. K is the ratio of gas thermal conductivity k based on translational energy over particle thermal conductivity $k_p = 0.6\ \mathrm{W/(m\,K)}$, and K_n is the Knudsen number. Additionally, C_s, C_m, and C_t are constants with values of 1.17, 1.14, and 2.18, respectively.

The tensor form of the Saffman lift force $F_{L,i}$ can be given as (Li and Ahmadi, 1992)

$$F_{L,i} = m_p \frac{2K\nu^{\frac{1}{2}} d_{ij}}{S d_p (d_{lk} d_{kl})^{\frac{1}{4}}}(u_j - u_{p,j}), \tag{22}$$

where $K = 2.594$ is the constant coefficient for the Saffman lift force, ν represents the kinematic viscosity, S is the ratio of particle density to fluid density, and d_{ij} is the deformation rate tensor, which is defined as

$$d_{ij} = \frac{1}{2}\left(\frac{\partial u_i}{\partial x_j} + \frac{\partial u_j}{\partial x_i}\right). \tag{23}$$

C. Initial and boundary conditions

1. Boundary conditions for gas carriers

To investigate the generality of H_2–O_2 gas mixture's influence on inhaled medicinal particles delivery into distal airways, i.e., downstream to G13, three inhalation–exhalation sinusoidal waveforms were applied as the inlet boundary conditions at the mouth opening (see Fig. 2) with different BPMs (i.e., 12, 16, and 20 times per min), representing patient's breathing conditions with a fixed tidal volume of 500 ml. The inhalation and exhalation time duration ratio was set as 1:2. For each CFPD simulation in this study, three inhalation–exhalation cycles were simulated under the three designated BPMs mentioned above, with the corresponding periods [i.e., breath cycle time (BCT) = 5, 3.75, and 3 s], respectively. Additionally, in each CFPD

simulation, particles were injected at the start of the third inhalation–exhalation cycle. Inhaled air temperature was set as the ambient indoor temperature at 25 °C. Airway walls were assumed stationary and non-slip in this study, and the airway wall temperature was set as the human body temperature (i.e., 37 °C). An outlet-vent boundary condition was assigned at the G13 terminal, with a gauge pressure of 0 Pa and a temperature of 37 °C.

2. Boundary conditions for particles

Particles were injected into the mouth opening at the end of the second inhalation–exhalation cycle and released four times. The first release was at a physical flow time of 2BCT + 0.01 s, where T is the period of one complete breath. Another three releases proceeded with a time interval of 0.01 s. A total of 100 000 particles were designated for each simulation case, and a single release was embedded with 25 000 particles. Since Stokes–Cunningham drag law was employed in this study [see Eq. (16)], $C_c = 1.16$, 1.04, and 1.02 were employed for simulations using air as the carrier when carrying the particles with the sizes of 1, 5, and 10 μm, respectively. For simulations using H_2–O_2 gas mixture as the carrier, $C_c = 1.24$, 1.05, and 1.02 were employed for simulations with the particle sizes of 1, 5, and 10 μm, respectively.

At the mouth opening, particles were assigned to escape during exhalation. Particles were designated to be trapped at the airway walls. It means once the distance between the centers of the particles and the wall is less than the particle radius, they are considered deposited. At the G13 airway openings, escaped boundary conditions were assigned for particles.

D. Numerical setup

CFPD simulations were performed using Ansys Fluent 2025 R2 (Ansys, Inc., Canonsburg, PA) with 48 parallel solver processors on a local HP Z840 workstation (Intel® Xeon® Processor E5–2690W v4 with dual processors, 28 cores, 56 threads, and 256 GB RAM). With the flow time step equal to 0.001 s, it costs ~48, 60, and 80 h to complete the simulations for three inhalation–exhalation cycles with BPM = 20, 16, and 12, respectively. The pressure–velocity coupling was achieved using the finite volume method with a Semi-Implicit Method for Pressure Linked Equations (SIMPLE) scheme. The least-squares cell-based (LSCB) method was employed to calculate cell-average gradients. In addition, a second-order scheme was used for pressure discretization. A second-order upwind approach for the discretization of momentum, turbulence kinetic energy, specific dissipation rate, specific species, and energy in both time and space. It is considered that the simulations have converged when all residuals are below 1×10^{-4}. In-house user-defined functions (UDFs) and MATLAB scripts were employed for solver customization to achieve the following capabilities, i.e.:

(1) Generating particle injection files,
(2) Defining the transient sinusoidal inhalation–exhalation waveforms at the mouth opening,
(3) Specifying the DPM time step, and
(4) Post-processing particle deposition data along the respiratory route of the lung, as well as wall shear stress (WSS) on the airway wall.

E. Particle delivery efficiency

The regional deposition of inhaled particles in human respiratory systems, and the particles across G13 terminals, can be quantified by regional deposition fractions (RDFs), which can be defined as

$$DF = \frac{\text{Number of deposited particles in a specific region}}{\text{Number of total particles inhaled}}. \quad (24)$$

F. CFPD model validation

The CFPD model employed in this study was validated by comparisons with benchmark experimental data on pulmonary airflow field and regional particle deposition. Details of the validations can be secured in the existing publications (Feng *et al.*, 2016; 2015; 2017; Haghnegahdar *et al.*, 2019). Nevertheless, there are still additional assumptions made during the simulation and post-processing stages, i.e.:

(1) Owing to the unavailable experimental data for the absorption dynamics of the gases from G13 to the alveoli, it was assumed that the gas compositions of the backflow at G13 terminals during the subsequent exhalation phases were updated to be identical to the gas composition at each G13 terminal opening at the end of inhalation phases.
(2) Particles that exit from G13 terminals were assumed to be deposited 100% in G14-to-alveoli regions, i.e., no particles can reenter the mouth-to-G13 domain after escaping.
(3) The dependency of viscosity, thermal conductivity coefficient, diffusivity coefficient, and heat capacity of gases on temperature was not considered in this study. Since the main factor of the density difference between air and the H_2–O_2 gas mixture, the influence of the factors mentioned above was negligible.
(4) The Soret effect in the continuous phase was neglected due to the small temperature gradient in the airway flows, which has been numerically validated in this study (see supplementary material).

III. RESULTS AND DISCUSSION

A. Gas flow patterns: Air vs H_2–O_2 gas mixture

Gas flow regimes in human respiratory systems contain laminar–turbulence–relaminarization transition flow (Zhao *et al.*, 2021) during the inhalation–exhalation process, which strongly impacts the transport and deposition of inhaled aerosolized particles. Because inspiratory flow patterns play a dominant role in inhaled aerosolized particle transport, this study mainly focused on the flow structure differences between using the two gas carriers. Specifically, to reveal the key distinguished flow characteristics in both air and H_2–O_2 gas mixture, the velocity flow fields (i.e., normalized velocity magnitude $\|\vec{u}\|^*$ at two representative time stations, i.e., t = 2BCT + 1/12BCT (at the half of the peak inhalation flow rate) and t = 2BCT + 1/6BCT (at the peak inhalation flow rate) were selected as the comparisons under investigated three breathing frequencies of 12, 16, and 20 BPM, respectively (see Figs. 3 and 4). $\|\vec{u}\|^*$ was calculated by $\|\vec{u}\|^* = \frac{\|\vec{u}\|}{\|\vec{u}\|_{ref}}$, in which $\|\vec{u}\|_{ref}$ is the average velocity magnitude on the mouth opening at the peak inhalation instant (i.e., t = 2BCT + 1/6BCT). As shown in Figs. 3 and 4 through the normalized velocity magnitude $\|\vec{u}\|^*$ contours, and in Fig. 5 with tangential velocity vectors, all six cases exhibit similar

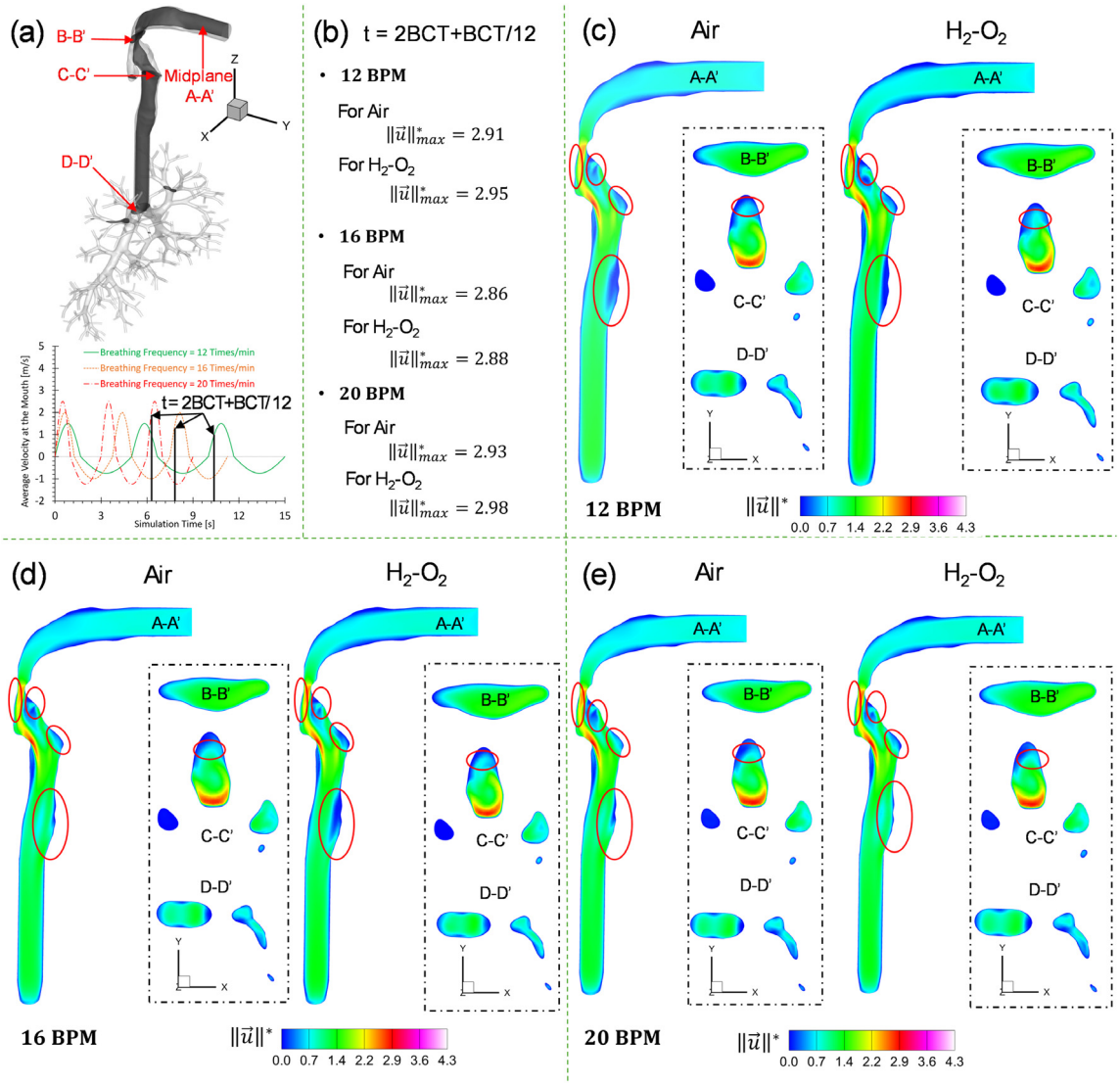

FIG. 3. Comparisons of air and H_2–O_2 gas mixture in $\|\vec{u}\|^*$ distributions on selected planes at t = 2BCT + BCT/12 with different BPMs: (a) selected planes and time instant, (b) $\|\vec{u}\|^*_{max}$ values with three BPMs, (c) $\|\vec{u}\|^*$ distributions at BPM = 12, (d) $\|\vec{u}\|^*$ distributions at BPM = 16, and (e) $\|\vec{u}\|^*$ distributions at BPM = 20.

overall flow distribution patterns. Noticeable changes can be observed with the transient inhalation flow rate increases from t = 2BCT + 1/12BCT to t = 2BCT + 1/6BCT (i.e., at the peak inhalation flow rate) in the selected planes (i.e., A–A′, B–B′, C–C′, and D–D′) with both gas carriers at the three breathing patterns. The highlighted regions marked in red circles on the midplane A-A′ and plane C-C′ across the glottis region shown in Figs. 3(c)–3(e) and 4(c)–4(e) reveal that the velocity fluctuations due to mouth and laryngeal jets and the wake recirculation in the glottis region were stronger in the H_2–O_2 gas mixture than air, more explicitly shown in Figs. 5 and 6 for turbulence kinetic energy (TKE) distributions. It is interesting to observe that, with the same breathing patterns, the maximum $\|\vec{u}\|^*$, denoted as $\|\vec{u}\|^*_{max}$, and shown in Figs. 3(b) and 4(b), with H_2–O_2 gas mixture cases are higher than that with air. For example, at the peak inhalation flow and BPM = 20 [see Figs. 4(b) and 4(e)], $\|\vec{u}\|^*_{max} = 4.23$ was obtained at near the glottis region in the H_2–O_2 gas mixture case, which is higher than the registered $\|\vec{u}\|^*_{max} = 4.13$ with air. Higher $\|\vec{u}\|^*_{max}$ using H_2–O_2 gas mixture indicates more unevenness of the flow distributions in the glottis region than air. This is due to the lower dynamic viscosity of the H_2–O_2 gas mixture (i.e., 1.24×10^{-5} Pa s) compared to air (i.e., 1.84×10^{-5} Pa s). Such lower dynamic viscosity generates less viscous dissipation and mixing, leading to more skewed velocity distributions. However, more skewed velocity distributions do not necessarily indicate greater turbulence near the airway wall, since the H_2–O_2 gas mixture has a much lower density than air.

Indeed, it is worth noting that the major difference between air and H_2–O_2 the gas mixture is the density. Employing the ideal gas law [i.e., Eqs. (6) and (7)], the density of air and H_2–O_2 gas mixture can be

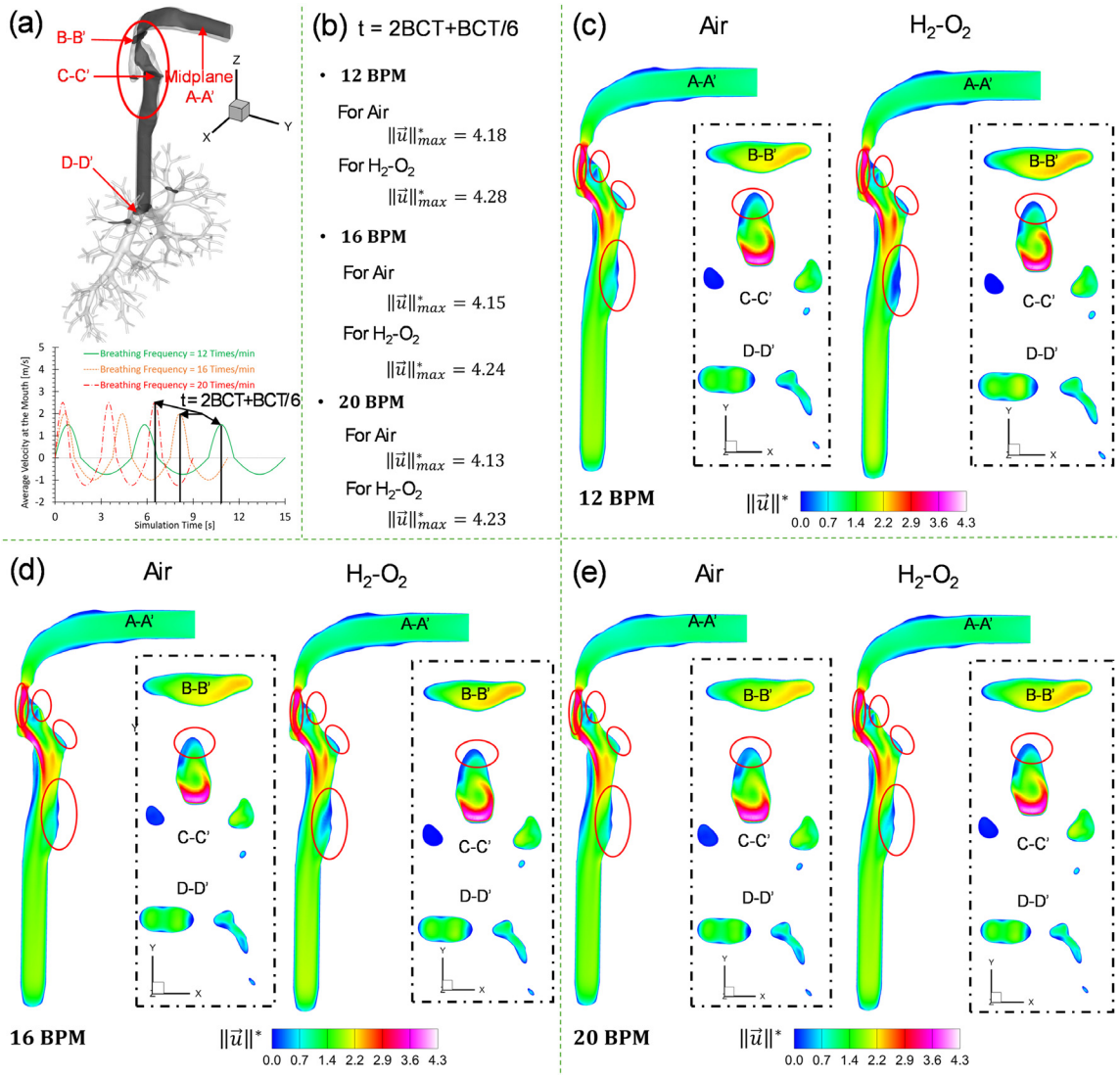

FIG. 4. Comparisons of air and H_2–O_2 gas mixture in $\|\vec{u}\|^*$ distributions on selected planes at the peak inhalation flow rate t = 2BCT + BCT/6 with different BPMs: (a) selected planes and time instant, (b) $\|\vec{u}\|^*_{max}$ values with three BPMs, (c) $\|\vec{u}\|^*$ distributions at BPM = 12, (d) $\|\vec{u}\|^*$ distributions at BPM = 16, and (e) $\|\vec{u}\|^*$ distributions at BPM = 20.

calculated, i.e., 1.18 and 0.49 kg/m^3 at the room temperature, respectively. Accordingly, with the same flow velocity at the room temperature, the Reynolds number ratio between air and H_2–O_2 gas mixture is 1.68. Such a fact indicates that when the drug particles are transported from the mouth open to the distal airways, using H_2–O_2 gas mixture as the carrier can potentially reduce the turbulence dispersion induced particle deposition than using air due to the relatively low Reynolds number. The reduction of turbulence intensity can also be demonstrated in Figs. 5 and 6. As visualized in Figs. 5(c)–5(e) and 6(a)–6(c), explicitly demonstrated in Fig. 5(b), TKE_{Max} values with H_2–O_2 gas mixture are all lower than with air under three breathing patterns. The same comparison can be found in the surface-averaged TKE and volume-averaged TKE as well. As illustrated in Table II, at the selected two instants (i.e., t = 2BCT + 1/12BCT and t = 2BCT + 1/6BCT), the surface-averaged TKE at midplane A-A′ and volume-averaged TKE in the entire lung model (mouth-G13) with air were higher than with H_2–O_2 mixture at the investigated three BPMs.

Furthermore, since the gas density will change with local temperature distributions, the spatial distributions of gas densities on the midplane A-A′ are also presented with three different breathing patterns at the peak inhalation flow rate [see Figs. 7(a)–7(c)]. Associated with Fig. 7, Figs. 8(a)–8(c) visualize the gas temperature distributions on the midplane A-A′. As shown in Figs. 7(a)–7(c), the gas density decreases from the mouth to the trachea as the gas warms progressively through heat exchange with the airway walls maintained at body temperature during their transport downstream in the upper airway and further into the TB tree [see Figs. 8(a)–8(c)]. When moving further downstream to G1, gas carrier density tends to reach uniform, i.e.,

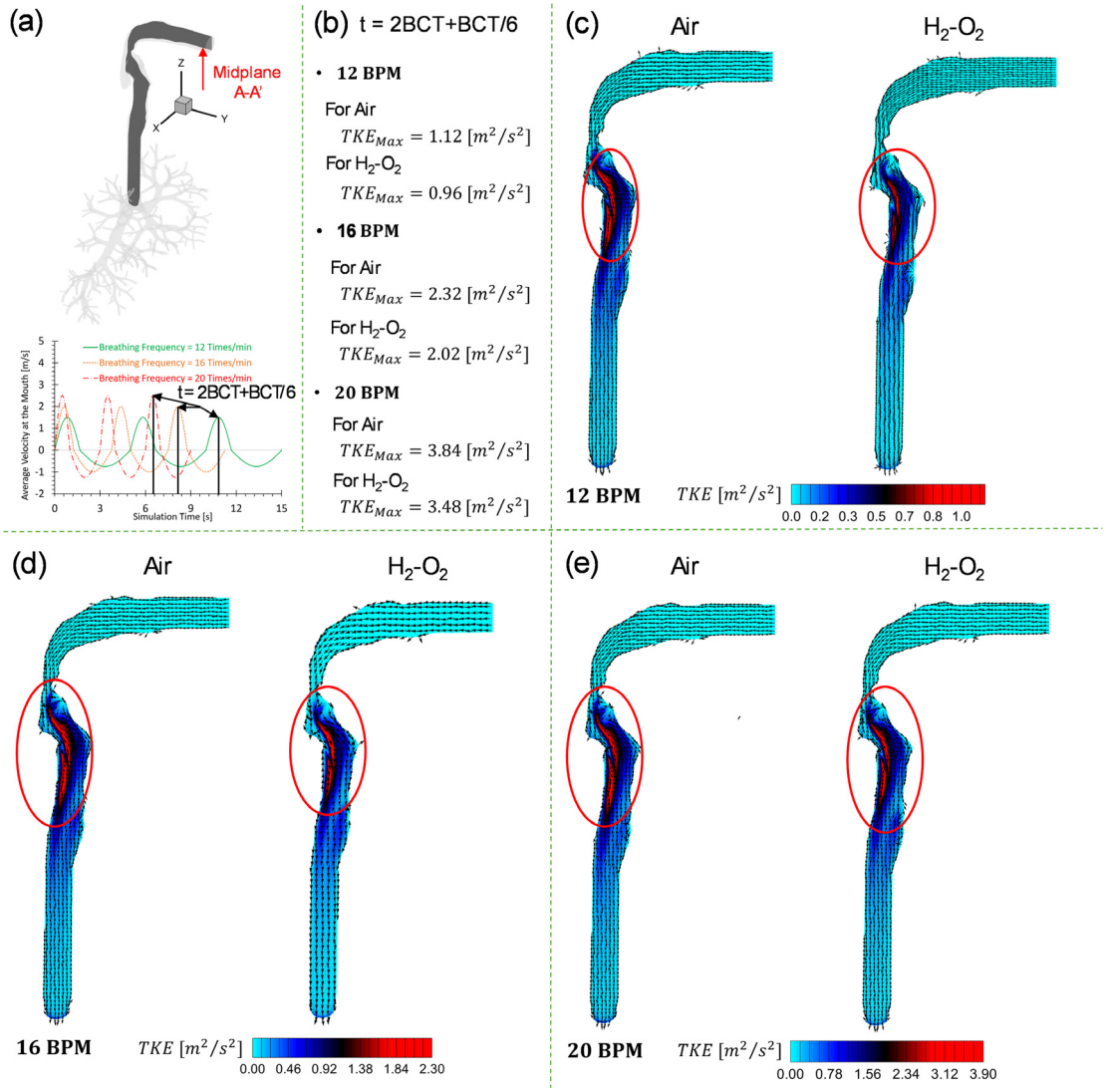

FIG. 5. Comparisons of air and H_2–O_2 gas mixture in TKE and tangential velocity vectors on the midplane A-A′ at the peak inhalation flow rate t = 2BCT + BCT/6: (a) selected midplane A-A′ and time instant t = 2BCT + BCT/6, (b) TKE_{Max} values with different BPMs, (c) TKE and tangential velocity vector distributions at BPM = 12, (d) TKE and tangential velocity vector distributions at BPM = 16, and (e) TKE and tangential velocity vector distributions at BPM = 20.

0.47 kg/m^3 for H_2–O_2 gas mixture and 1.13 kg/m^3 for air, respectively. However, at the peak flow rate instant (t = 2BCT + 1/6BCT), neither H_2–O_2 gas mixture nor air, the density field still has not achieved a "quasi-steady-state" at the end of G1 (see red-circled regions in Fig. 7). As shown in Figs. 7 and 8, the density and temperature of gases with higher BPM values require a longer distance to reach a quasi-steady-state within the respiratory system. At a fixed tidal volume of 500 ml, a higher BPM results in a higher flow rate, thereby increasing the distance required for the gas density to stabilize. The observed density variations along the airways can be primarily attributed to the temperature difference between the inhaled gas and the airway walls (see Fig. 8). The cooler gas entering through the open mouth is progressively heated by the warmer airway walls until body temperature is reached. Notably, the H_2–O_2 gas mixture attains body temperature earlier than air under all BPM conditions investigated, which is due to H_2–O_2 gas mixture having higher thermal conductivity and lower density (see Table I). It suggests that heat transfer between the H_2–O_2 gas mixture and the airway wall is more efficient than that of air. Consequently, the smaller temperature gradient in the H_2–O_2 gas mixture reduces the thermophoretic force acting on inhaled particles, which is expected to alter their transport and deposition behavior within the airways.

Additionally, previous investigation revealed that excessively high wall shear stress (WSS) can lead to several specific types of damage and related complications in the airways (Foncerrada *et al.*, 2018; Reper and Heijmans, 2015). In this study, WSS and pressure distributions at the peak flow rate (t = 2BCT + BCT/6) were visualized and

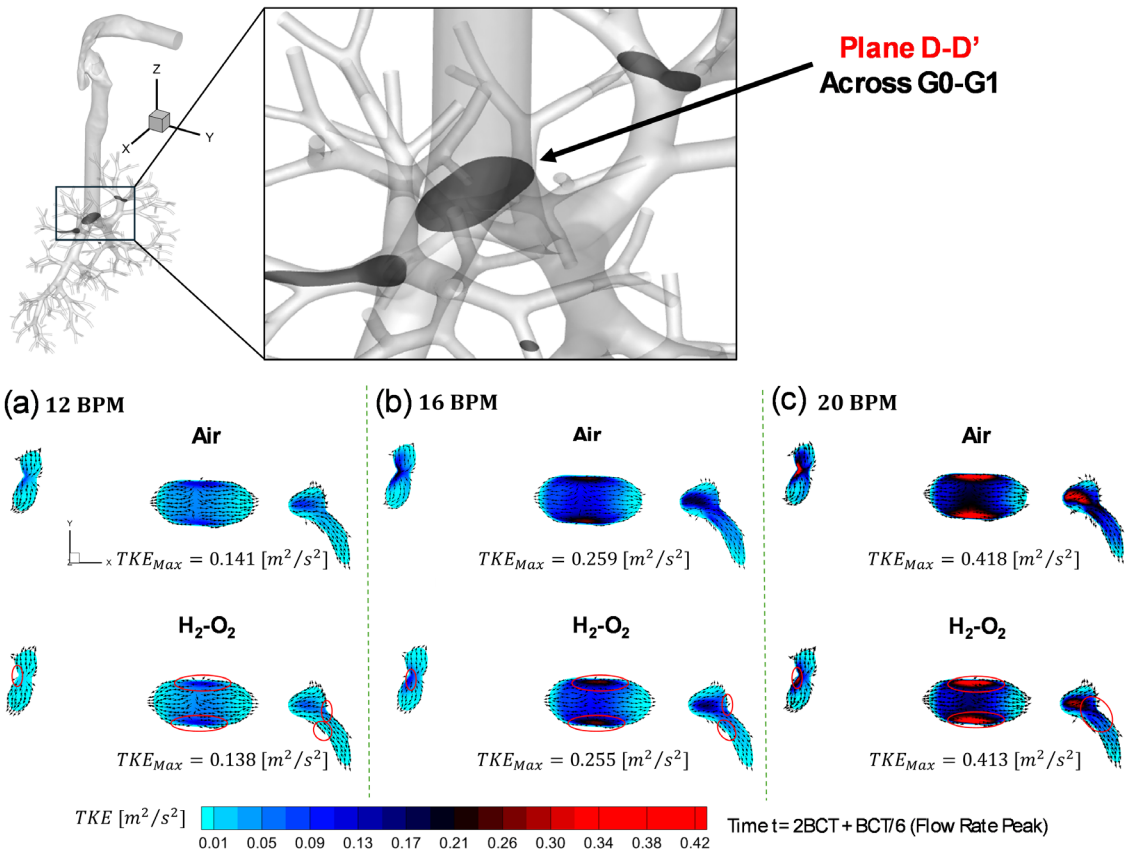

FIG. 6. Comparisons of air and H_2–O_2 gas mixture in TKE distributions on plane D-D′ under different BPMs at the peak inhalation flow rate t = 2BCT + BCT/6: (a) BPM = 12, (b) BPM = 16, and (c) BPM = 20.

compared between the two inhalation therapy strategies using air vs H_2–O_2 gas mixture, as shown in Figs. 9 and 10, respectively. Using 20 BPM as an example, it can be observed that, relative to conventional air used as the inhaled medicinal particle carrier, the H_2–O_2 gas mixture can potentially provide a milder mechanical environment within the human lung system, characterized by lower WSS acting on the airway walls and a smaller pressure drop (Δp) from the mouth to the distal airways. At this time instant, the WSS_{max} of 2.06 Pa was observed in the laryngopharyngeal region [circled in Fig. 9(c)] using H_2–O_2 gas mixture as the particle carrier, which was substantially lower than the corresponding value of 3.72 Pa for air. A similar trend was observed in the pressure drop, with Δp values of 31.6 Pa for the H_2–O_2 gas mixture and 71.3 Pa for air, respectively [see Fig. 10(c)]. These findings suggest that inhalation with an H_2–O_2 gas mixture may reduce airway mechanical stress and flow resistance and thereby encourage the adoption of such less invasive ventilation procedures to alternate the currently use (Nof *et al.*, 2020), with the advantages of minimizing the potential for epithelial irritation or tissue damage during breathing or aerosol drug delivery.

TABLE II. Surface-averaged TKE (m^2/s^2) on midplane A-A′ and volume-averaged TKE (m^2/s^2) at time t = 2BCT + BCT/12 and t = 2BCT + BCT/6.

		BPM = 12		BPM = 16		BPM = 20	
Time	Locations	Air	H_2–O_2	Air	H_2–O_2	Air	H_2–O_2
2BCT + BCT/12	Midplane A-A′	3.18×10^{-2}	1.11×10^{-2}	7.77×10^{-2}	5.16×10^{-2}	1.46×10^{-1}	1.16×10^{-1}
	Entire lung	1.70×10^{-2}	5.80×10^{-3}	4.51×10^{-2}	2.66×10^{-2}	8.75×10^{-2}	6.48×10^{-2}
2BCT + BCT/6	Midplane A-A′	1.06×10^{-1}	8.49×10^{-2}	2.41×10^{-1}	2.04×10^{-1}	3.97×10^{-1}	3.51×10^{-1}
	Entire lung	5.94×10^{-2}	4.42×10^{-2}	1.36×10^{-1}	1.10×10^{-1}	2.30×10^{-1}	1.94×10^{-1}

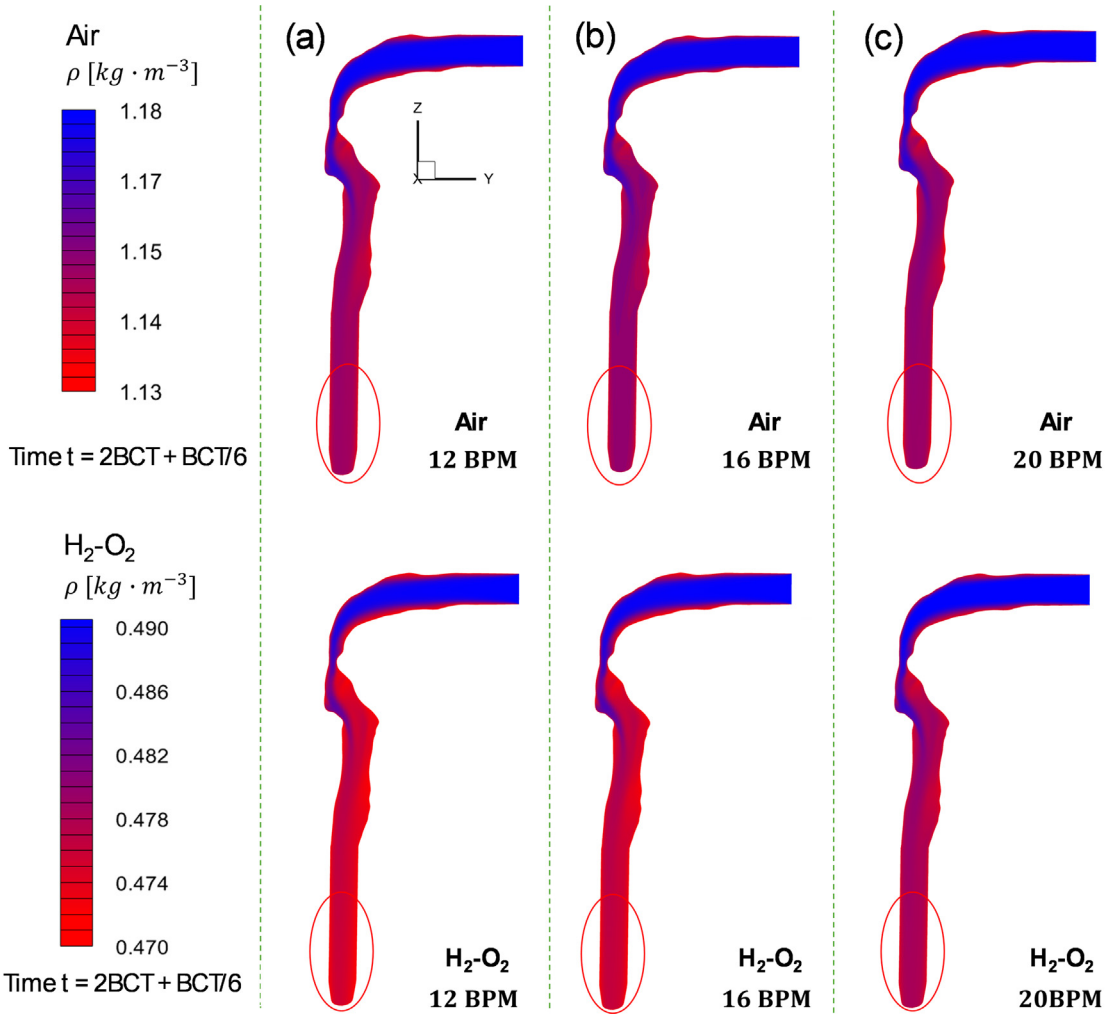

FIG. 7. Comparisons of air and H_2–O_2 gas mixture in density distributions on the midplane A-A′ at the peak inhalation flow rate t = 2BCT + BCT/6: (a) BPM = 12, (b) BPM = 16, and (c) BPM = 20.

B. Impact of gas carrier on particle transport and deposition

Following the analysis of flow dynamics and pressure characteristics, the investigation was extended to assess whether and then how the use of an H_2–O_2 gas mixture as a particle carrier offered greater potential than air for efficient drug delivery to the deep lung. To this end, the transport and deposition of 1, 5, and 10 μm particles within the human respiratory system were further analyzed and visualized under both carrier gases and three breathing patterns (12, 16, and 20 BPM).

Figures 11(a)–11(c) show the regional deposition fractions (RDFs) from G13 to alveoli at the end of the third breathing cycle, with multiple particle diameters, BPMs, as well as two different gas carriers. It can be found that using H_2–O_2 gas mixture can deliver more particles to the peripheral lung region (G13-to-alveoli) than using air for all particle sizes and breathing patterns tested. The enhancement of RDFs in the G13-to-alveoli region ranged from 9.16% [for 10 μm particles at 12 BPM shown in Fig. 11(a)] to 0.13% [for 1 μm particles at 12 BPM shown in Fig. 10(a)]. This improved delivery dose to the G13-to-alveoli region with the H_2–O_2 gas mixture was attributed to its lower density (see Fig. 7) and higher kinematic viscosity compared with air, which reduced the Reynolds number and consequently lowered the TKE (see Figs. 5 and 6) and the resultant turbulence dispersion effect and the induced particle deposition from mouth to G13. Specifically, as displayed in Figs. 6(a)–6(c) showing TKE distributions of the sliced plane D-D′ at the peak flow instant which details the velocity fluctuations at three bronchial bifurcations, the induced turbulence energy in the H_2–O_2 gas mixture at near wall regions (see red-circled region in Fig. 10) was much smaller than the same locations in the air, although the registered maximum TKE TKE_{Max} is close to each other in both fluid domains. For example, at the inhalation flow peak instant (i.e., t = 2BCT + BCT/6), as shown in Figs. 6(a)–6(c), $TKE_{Max} = 0.141$, 0.259, and 0.418 m^2/s^2 on D-D′ were found for cases using air as the carriers with 12, 16, and 20 BPM, respectively. In

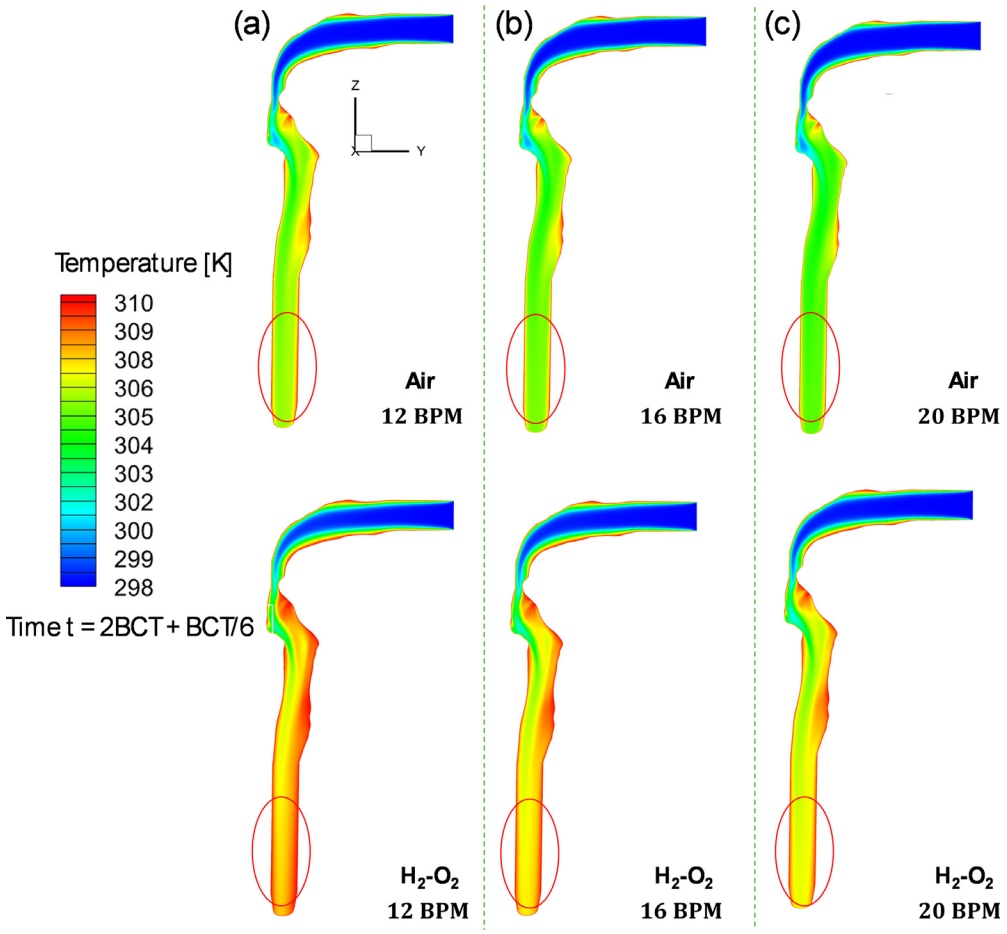

FIG. 8. Comparisons of air and H_2–O_2 gas mixture in temperature distributions on the midplane A-A′ at the peak inhalation flow rate t = 2BCT + BCT/6: (a) BPM = 12, (b) BPM = 16, and (c) BPM = 20.

contrast, TKE_{Max} = 0.138, 0.255, and 0.413 m^2/s^2 on D-D′ were documented for the H_2–O_2 gas mixture cases for 12, 16, and 20 BPM, which are all lower than air cases. As a result, the reduction in TKE will lead to the decrease in inertial impaction and turbulence dispersion-induced particle deposition in the upper airway, and more particles can potentially transport into the peripheral lung region using the H_2–O_2 gas mixture as the carrier than air.

The potential of the H_2–O_2 gas mixture to deliver more particles to the peripheral lung region than air can also be demonstrated by the RDFs. Figures 12(a)–12(c) compare RDFs at the end of third breathing circles with multiple particle diameters and BPMs between using air and H_2–O_2 gas mixture as the carrier in the categorized five airway regions (see Fig. 1). Specifically, the five airway regions are as follows: the upper airway from mouth to trachea (M–T), tracheobronchial tree 1 (TB1) including the main trachea region to the left superior lobe and right superior lobe, TB2 involving the left inferior lobe, TB3 referring to the right inferior lobe, and local G13. It can be found that in Fig. 12 no matter how using both air carrier and H_2–O_2 carrier, as BPM increases from 12 to 20, RDF decreases accordingly at G0–G13 airway walls (i.e., TB1, TB2, TB3, and local G13), which is due to more particles deposited in the M–T region when increasing BPM. It can also be observed that RDFs in M–T, TB1, TB2, TB3, and local G13 using air as carriers are all higher than RDFs using H_2–O_2 gas mixture, except for some RDF comparisons in TB1, TB2, and local G13 for 10 μm particles shown in Figs. 12(a)–12(c). It means that, compared to using the H_2–O_2 gas mixture, although fewer particles with $d_p = 1$ and 5 μm can transport across the M–T region when using air, these particles have higher opportunities to be trapped by the regions of M–T, TB1, TB2, TB3, and local G13 due to stronger inertial impaction and turbulence dispersion. It is worth mentioning that under the drug particle administration scenario with $d_p = 10\,\mu$m, more drug particles were deposited on the three local regions (i.e., TB1, TB2, and local G13) using the H_2–O_2 gas mixture than air. For example, at BPM = 12 and $d_p = 10\,\mu$m, the comparisons using H_2–O_2 mixture gas vs air in RDFs are 17.10% vs 14.33%, 5.55% vs 4.69%, 0.97% vs 0.94% at TB1, TB2, and local G13, respectively. It is mainly due to the following factors. The primary factor is that, compared to using air, the dosed particles have more opportunities to travel through the M–T region using H_2–O_2 gas mixture, leading to the escaped particles from the M–T region in the H_2–O_2 gas mixture, resulting in more depositions on the

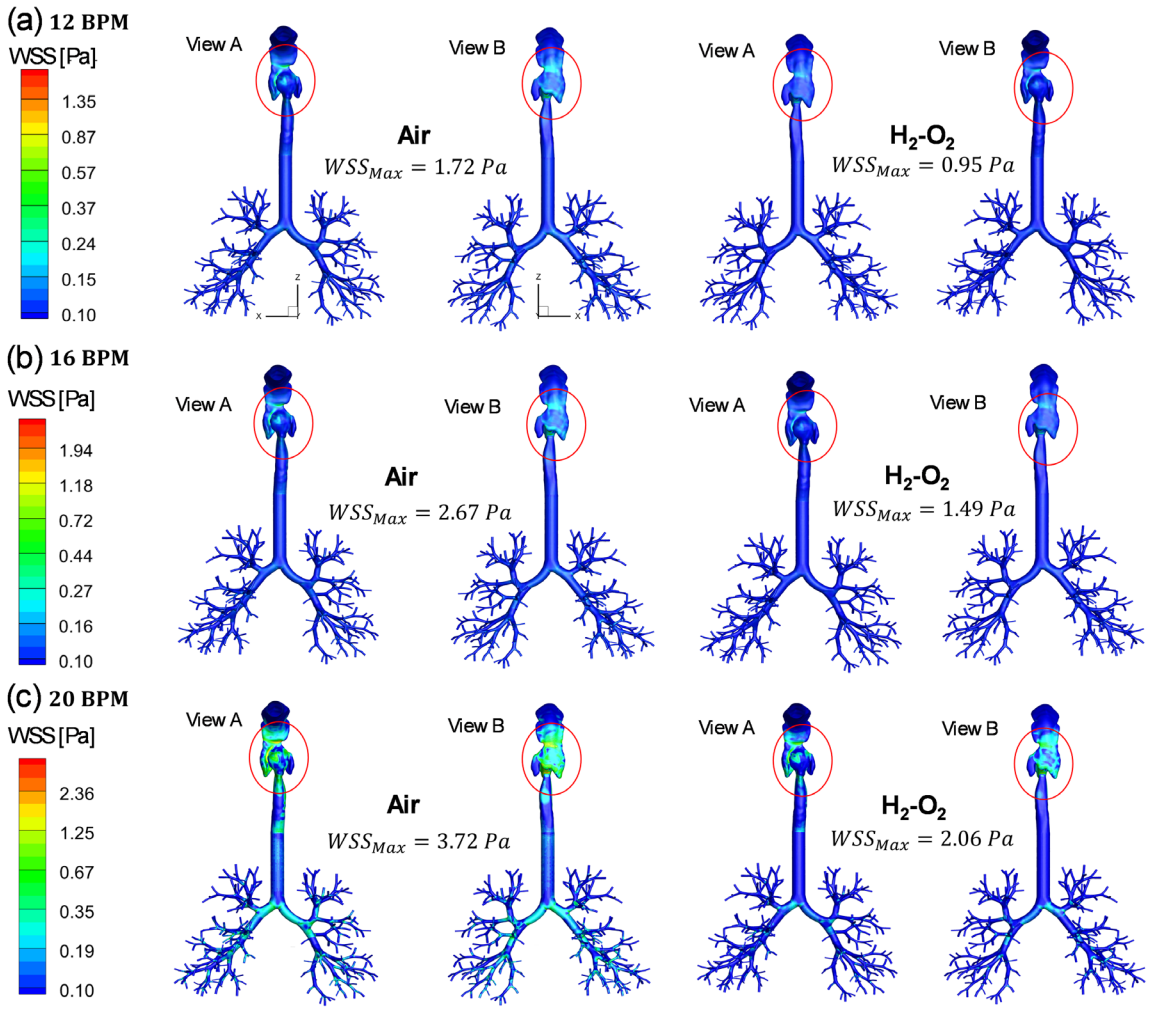

FIG. 9. Comparisons of air and H_2–O_2 gas mixture in WSS distributions on airway walls at the peak inhalation flow rate t = 2BCT + BCT/6: (a) BPM = 12, (b) BPM = 16, and (c) BPM = 20.

lower airways (TB1, TB2, TB3, and local G13). Uniquely, under this condition at the regions of TB1, TB2, and local G13, the inertial impaction and turbulence dispersion will play a secondary role, in terms of deposition consequence, although such a stronger factor induced by using air than H_2–O_2 gas mixture can lead to a single particle having a higher chance to be entrapped by the airway wall.

Overall, the comparisons in Figs. 11(a)–11(c) demonstrate that the H_2–O_2 gas mixture can effectively reduce particle deposition from the mouth to G13, thereby enhancing particle delivery to the G13-to-alveolar region across different particle sizes and breathing patterns. Despite the slightly increased RDFs observed with the H_2–O_2 gas mixture in certain regions [see Figs. 12(a)–12(c)], the overall conclusion remains consistent, i.e., the reduction in turbulence kinetic energy (TKE) decreases inertial impaction and turbulence–dispersion-induced particle deposition in the upper airways, enabling a higher number of particles to reach the peripheral lung regions when the H_2–O_2 gas mixture is used as the carrier.

Localized particle transport and deposition are visualized in Figs. 13–16, to further understand the underlying mechanisms of different gas carriers on pulmonary gas-particle flow dynamics. Specifically, localized particle deposition patterns are shown in Figs. 12(a)–12(c), colored by the particle residence time (PRT). It can be observed that (1) in the upper airway, concentrated particle deposition locations are the pharynx, larynx, and the bifurcating point between G0 and G1 due to the inertial impaction and turbulence dispersion; and (2) in the TB tree, the concentrated particle deposition locations are more scattered but mainly near the bifurcating points due to the interception effect. The localized deposition patterns clearly show that particle deposition in the upper airway (i.e., M–T region) using H_2–O_2 gas mixture as the carrier is less than in cases using air. Figures 14–16 visualize the distribution of suspending particles at three representative time stations, i.e., t = 2BCT + BCT/12, 2BCT + BCT/6, and 2BCT + BCT/3 at BPM = 12, 16, and 20, respectively. It is interesting to observe that at the end of the third inspiratory phase (i.e., t = 2BCT + BCT/3), more

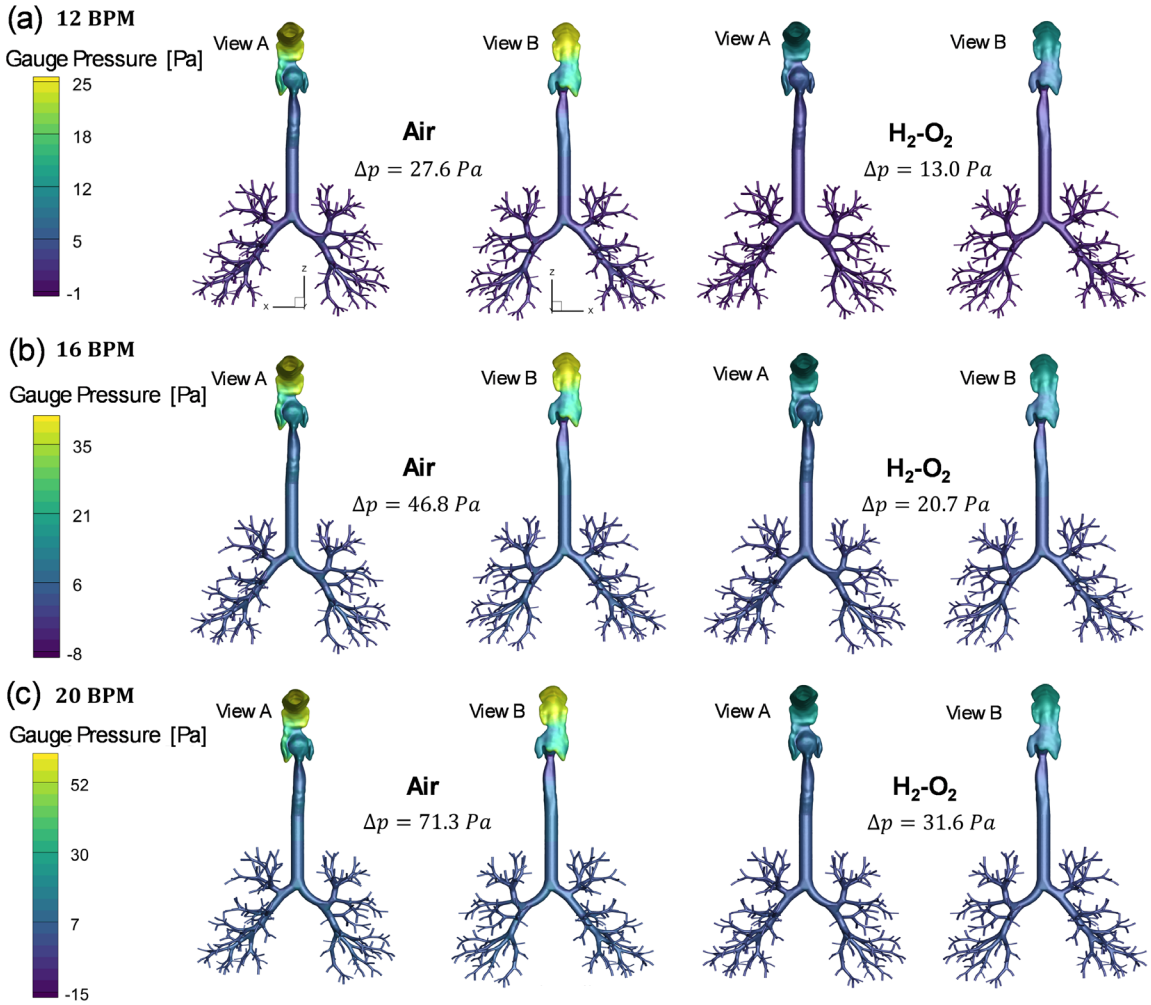

FIG. 10. Comparisons of air and H_2–O_2 gas mixture in pressure drop distributions on airway walls at the peak inhalation flow rate t = 2BCT + BCT/6: (a) BPM = 12, (b) BPM = 16, and (c) BPM = 20.

particles carried by the H_2–O_2 gas mixture were suspending in the lung regions (i.e., M–T and TB1) than air. Such observations also support that fewer particles deposited in the upper airway using the H_2–O_2 gas mixture as the carrier than air.

Based on the comparisons of RDFs and localized particle suspension and deposition above, it can be concluded that an H_2–O_2 gas mixture with a volume ratio 2:1 as the carrier gas for inhaled medicinal particles can potentially lead to a higher delivered dose in the peripheral lung than air.

C. Impact of breathing patterns (BPM) on particle transport and deposition

Since Sec. III B demonstrates that particle deposition exhibits similar spatial distributions of particle transport and deposition in both air and H_2–O_2 gas mixture environments (see Figs. 11–16), this section, as well as Sec. III D, focuses exclusively on the effects of breathing patterns and particle diameters on particle transport dynamics using cases with H_2–O_2 gas mixture as the carrier.

To investigate the influence of the breathing pattern on the particle transport and deposition dynamics in the respiratory mouth-to-G13 airway with H_2–O_2 gas mixture as the carrier, three transient inhalation–exhalation waveforms (see Fig. 2) with the same tidal volume and different BPMs (i.e., 12, 16, and 20) were employed.

As shown in Figs. 11 and 12, BPM has noticeable influences on RDFs. As BPM increases from 12 to 20 with the same tidal volume and inhalation-to-exhalation time duration ratio, the likelihood of particles reaching the peripheral lung (i.e., G13-to-alveoli region) decreases, with the reduction ranging from 0.26% for 1 μm particles to 30.69% for 10 μm particles [see Figs. 11(a)–11(c)]. Such a trend is due to higher inertial impaction and turbulence dispersion induced deposition, especially in the upper airway [i.e., M–T region shown in Figs. 12(a)–12(c) and 13], with the increase in BPM. Specifically, with a shorter duration of the inhalation and the same tidal volume per

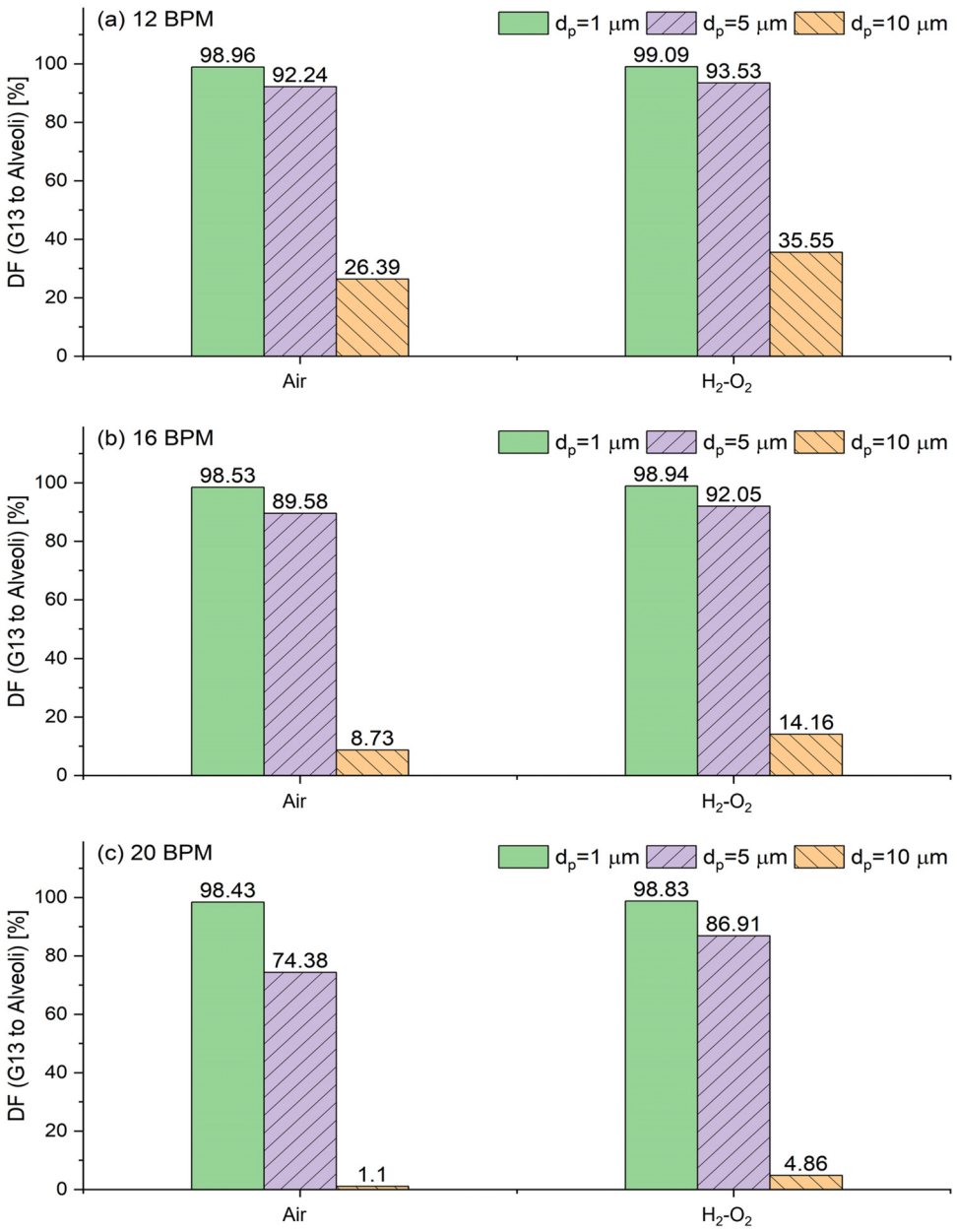

FIG. 11. Comparisons of particle RDFs in the distal airways (i.e., G13-to-alveoli region) carried by air vs H_2–O_2 gas mixture with different BPMs at the end of the third breathing cycles: (a) BPM = 12; (b) BPM = 16; and (c) BPM = 20.

breath, the peak inspiration flow velocity at the mouth opening increases from 1.5 to 2.5 m/s (see Fig. 2) when BPM increases from 12 to 20. Accordingly, higher turbulence intensity was generated with the higher Reynolds number for BPM = 20 compared with the other two breathing conditions. Quantitatively, the Reynolds number at an equivalent relative time point within each breathing cycle increases by a factor of ∼1.67 as BPM rises from 12 to 20. Correspondingly, the maximum turbulence kinetic energy (TKE_{Max}) at the midplane A-A′ increases by ∼3.6 times at the peak inspiratory flow (see Fig. 5). Therefore, the increase in instantaneous velocity and turbulence intensity at higher BPM amplifies inertial impaction and turbulence dispersion effects, thereby promoting enhanced particle deposition throughout upper airway (i.e., M–T region) and decreasing the delivered dose to peripheral lung in this study (i.e., G13-to-alveoli). The increased particle deposition in the upper airway with higher BPM can also be observed from the localized particle deposition patterns shown in Figs. 13(a)–13(c).

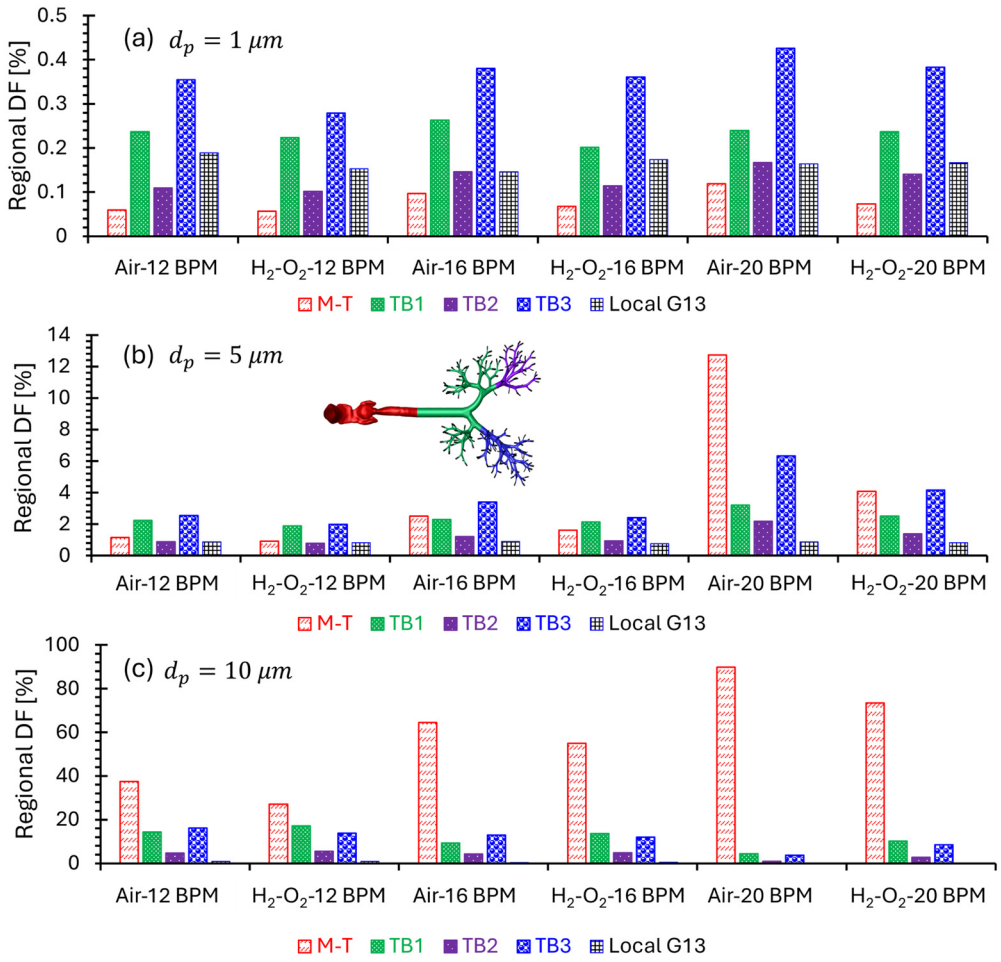

FIG. 12. Comparisons of air and H_2–O_2 mixture effects on particle RDFs from mouth to G13 with different particle sizes at the end of the third breathing cycles: (a) $d_p = 1\ \mu$m, (b) $d_p = 5\ \mu$m, and (c) $d_p = 10\ \mu$m.

More generally, in both air and H_2–O_2 gas mixture environments, a lower BPM provides less inertial impaction and turbulence dispersion, allowing more particles to transport into peripheral lungs, especially for smaller fine particles and BPM = 12 (see Figs. 11–13). Specifically, under BPM = 12, ~27% of inhaled particles with $d_p = 10\ \mu$m were trapped within the M–T region, whereas at BPM = 20, this DF increased by about 1.7 times. This indicates that over 73% of the particles failed to pass beyond the G1 bifurcation into deeper airways, substantially diminishing targeted drug delivery efficiency to the peripheral lung. Such phenomena are visualized in Figs. 13–16, which show suspending particle transport dynamics at representative time stations, i.e., at half of the peak inhalation flow rate (t = 2BCT + BCT/12T), at the peak inhalation flow rate (t = 2BCT + BCT/6T), and at the end of inhalation (t = 2BCT + BCT/3T). Under higher BPM conditions, fewer suspended particles are observed in the upper airway (i.e., the M–T region) at t = 2BCT + BCT/12T due to the earlier disturbance on particles by turbulent flow structures, as illustrated in Figs. 15 and 16.

The trend mentioned above confirms that with the same tidal volume, a dosing strategy of "slow inhalation with longer duration" (i.e., lower BPM) is more effective for maximizing drug delivery to the peripheral lung regions (Borgström *et al.*, 2006; Usmani *et al.*, 2005; and Woodward and Fromen, 2024), providing a more efficient way to deposit drugs in the target area. Slower inhalation reduces inertial impaction and turbulence dispersion in the upper airways, allowing a larger fraction of particles to transport to the TB tree and potentially reach small airways.

D. Impact of particle size on particle transport and deposition

To figure out the particle size influence on transport and deposition dynamics of inhaled aerosolized drug particles in the respiratory airway model when using H_2–O_2 gas mixture as the carrier, three representative particle diameters (i.e., 1, 5, and 10 μm) were employed in this study. From Figs. 11 and 12, it can be observed and reconfirmed that the fine particle size plays a dominant role in their transport and

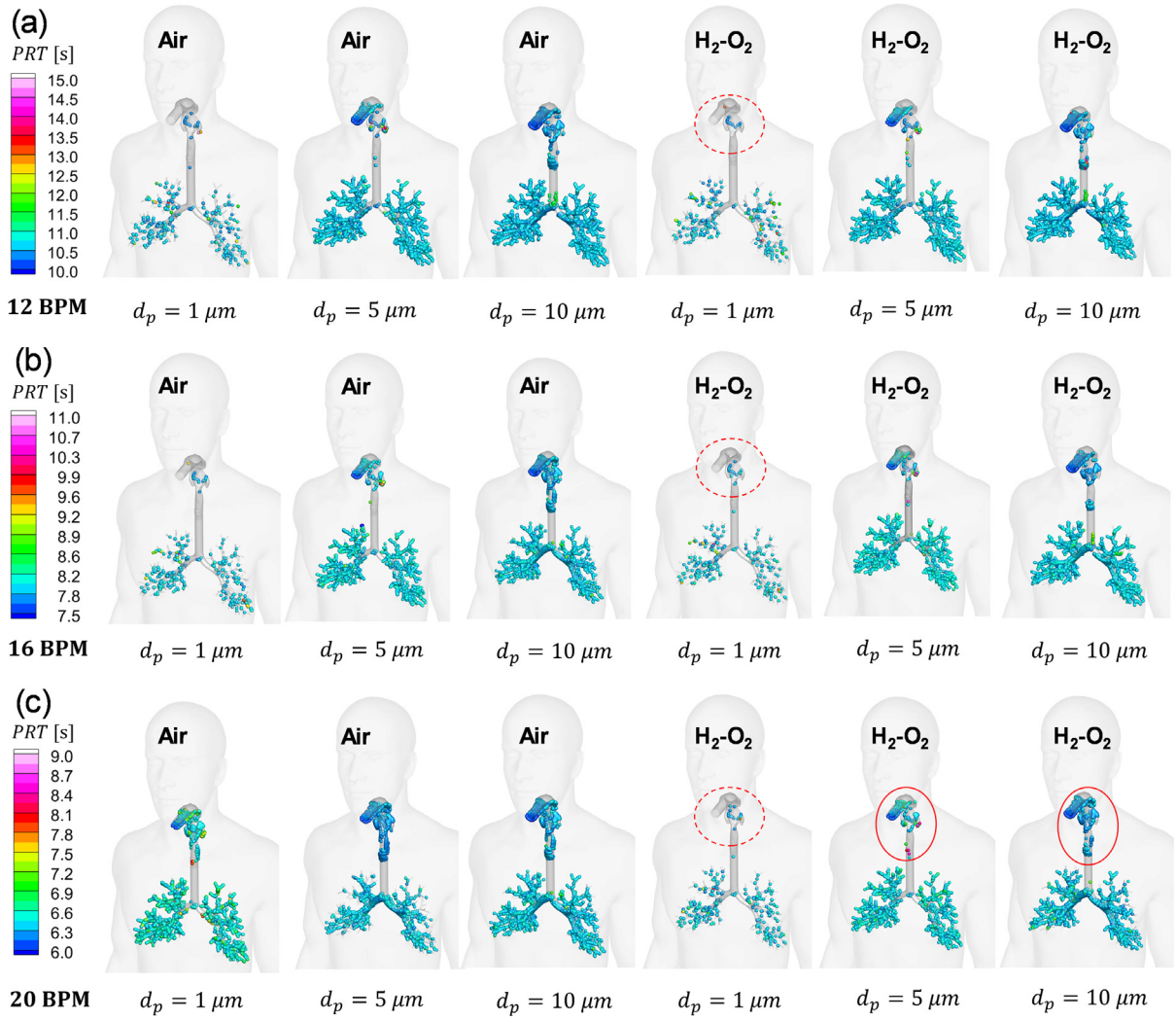

FIG. 13. Comparisons of air and H_2–O_2 gas mixture influence on localized particle deposition patterns under different BPMs at the end of the third breathing cycles: (a) BPM = 12, (b) BPM = 16, and (c) BPM = 20.

deposition in human respiratory systems. It can be found from Fig. 11 that with the increase in particle diameter from 1 to 10 μm, RDFs in the G13-to-aveoli region decrease accordingly. This is because, as the particle size increases, particle deposition from the mouth to G13 due to the dominant deposition mechanisms, i.e., inertial impaction and gravitational sedimentation, also increases.

Furthermore, Fig. 12 shows more details of RDFs in multiple regions from the mouth to G13 with the variation in inhaled particle sizes. The RDFs in M–T, TB1, TB2, TB3, and local G13 decrease monotonically with the increase in particle size due to the decrease in turbulence dispersion effect, as well as the enhanced inertial impaction and gravitational sedimentation, which are the dominant mechanisms for particle deposition in TB tree. The total DF from mouth to G13 also decreases monotonically with an increase in particle size.

Additionally, as illustrated in Fig. 13 (see red dashed circles), smaller particles (e.g., $d_p = 1\,\mu$m) rarely deposit in the M–T region, whereas larger particles ($d_p = 5$ and 10 μm) show concentrated deposition there. This strong particle size dependence can be explained using Eq. (12). Specifically, as particle size increases, the influence of surface forces (e.g., drag and lift forces) diminishes relative to body forces (e.g., gravity), leading to reduced aerodynamic responsiveness. As a result, larger particles have longer response time and are less capable of following rapid changes in airflow direction, making them more likely to impact and deposit in regions with abrupt flow deflections, such as the oropharynx, particularly near the back side and airway bifurcating points (see red solid circles in Fig. 13). It can also be observed from Figs. 11–13, large particles (e.g., $d_p = 5$ and 10 μm) seldom reach the deep lung, even when H_2–O_2 gas mixture is used as the carrier. Instead, they deposit predominantly in the upper airways, which can reduce drug delivery efficiency and, in some cases, cause unwanted local side effects (e.g., oropharyngeal deposition of corticosteroids leading to oral thrush). Therefore, despite the use of an H_2–O_2 gas mixture,

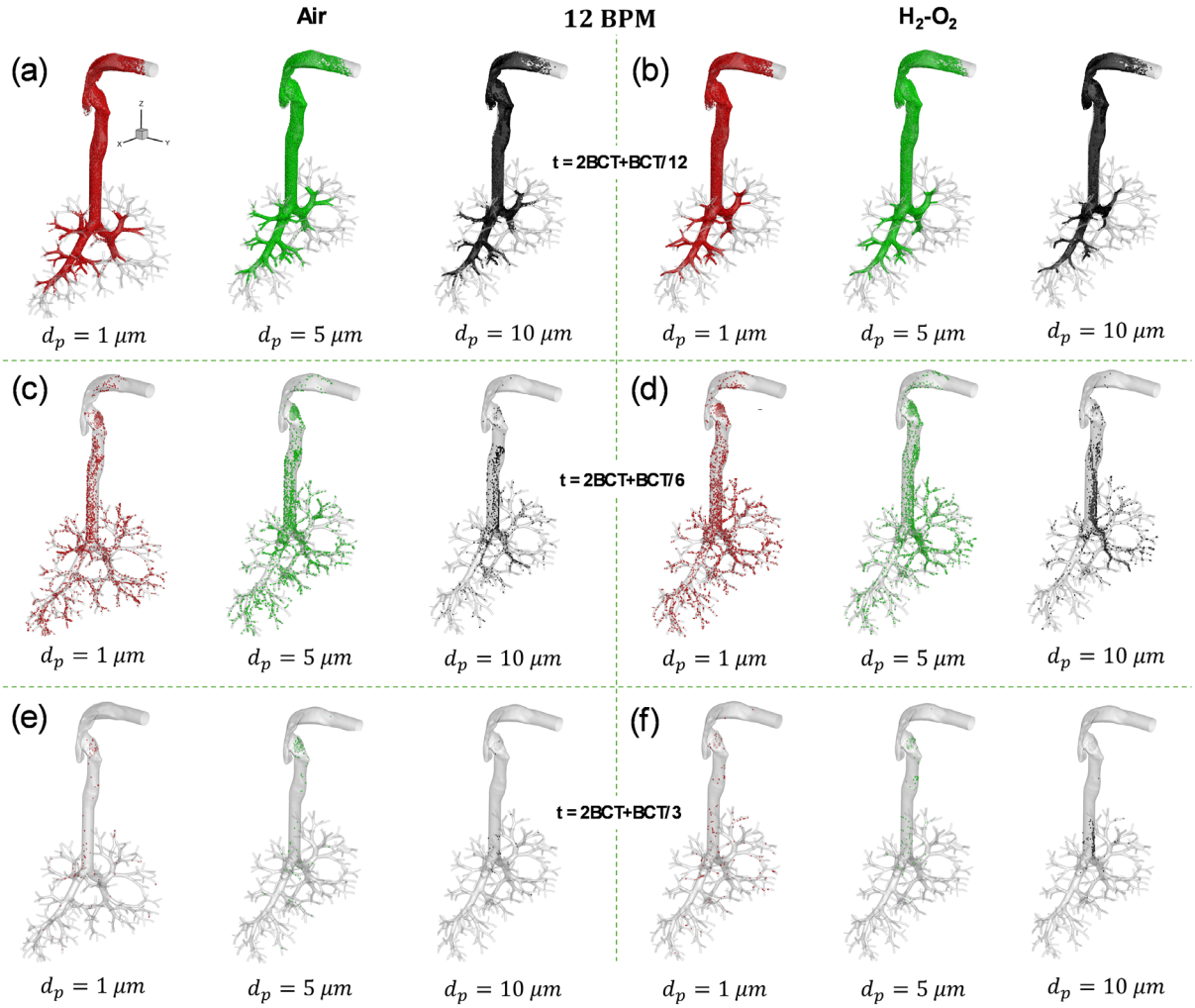

FIG. 14. Distributions of suspending particles at multiple time stations with BPM = 12: (a) t = 2BCT + BCT/12 with air, (b) t = 2BCT + BCT/12 with H_2–O_2 gas mixture, (c) t = 2BCT + BCT/6 with air, (d) t = 2BCT + BCT/6 with H_2–O_2 gas mixture, (e) t = 2BCT + BCT/3 with air, and (f) t = 2BCT + BCT/3 with H_2–O_2 gas mixture.

the improvement in targeted drug delivery to distal regions remains limited for larger particles (i.e., $d_p = 10\ \mu m$). Clinically, the findings from this study support the use of smaller particles (i.e., $d_p < 5\ \mu m$) to achieve efficient deposition in the peripheral lung.

Overall, the parametric analysis presented in Secs. III B–III D demonstrates that the highest RDFs in the G13-to-alveoli regions are obtained when using 1 μm particles at 12 BPM, with H_2–O_2 gas mixture as the carrier.

E. Potential physiological effects of H_2–O_2 gas as medicinal particle carriers

Since the composition of the H_2–O_2 gas mixture is apparently different from conventional carrier (i.e., air), the potentially introduced risks due to such changes to health should be discussed. Specifically, when using H_2–O_2 gas mixture, the volumetric fraction of inhaled O_2 will be increased to 33.3% compared with air (~21% of O_2), leading to the respiratory system in the presence of excess O_2. Previous investigations showed that breathing high concentrations of O_2 for an extended period can result in direct injuries to the lungs (Brubakk *et al.*, 2003), since overdosing reactive O_2 species could damage the alveolar cells and the capillary endothelium. This would further lead to several lung symptoms, such as inflammation (i.e., tracheobronchitis), shortness of breath, chest pain, and eventually pulmonary edema and fibrosis. This issue should be paid close attention to if a long-term therapy is projected to treat respiratory diseases such as COPDs (Mach *et al.*, 2011) when using H_2–O_2 gas mixture as the drug carrier. Nevertheless, in some patients with chronic CO_2 retention (e.g., severe COPD), higher O_2 concentration levels can reduce their "hypoxic drive" to breathe, leading to hypoventilation and worsening respiratory acidosis (Abdo and Heunks, 2012). H_2 is generally considered biologically inert at room temperature, but when administered as a medical gas, specific effects, namely, pharmacological effects in clinical practice, have been noted in previous investigations (Cole *et al.*, 2021; Ohta, 2014). When

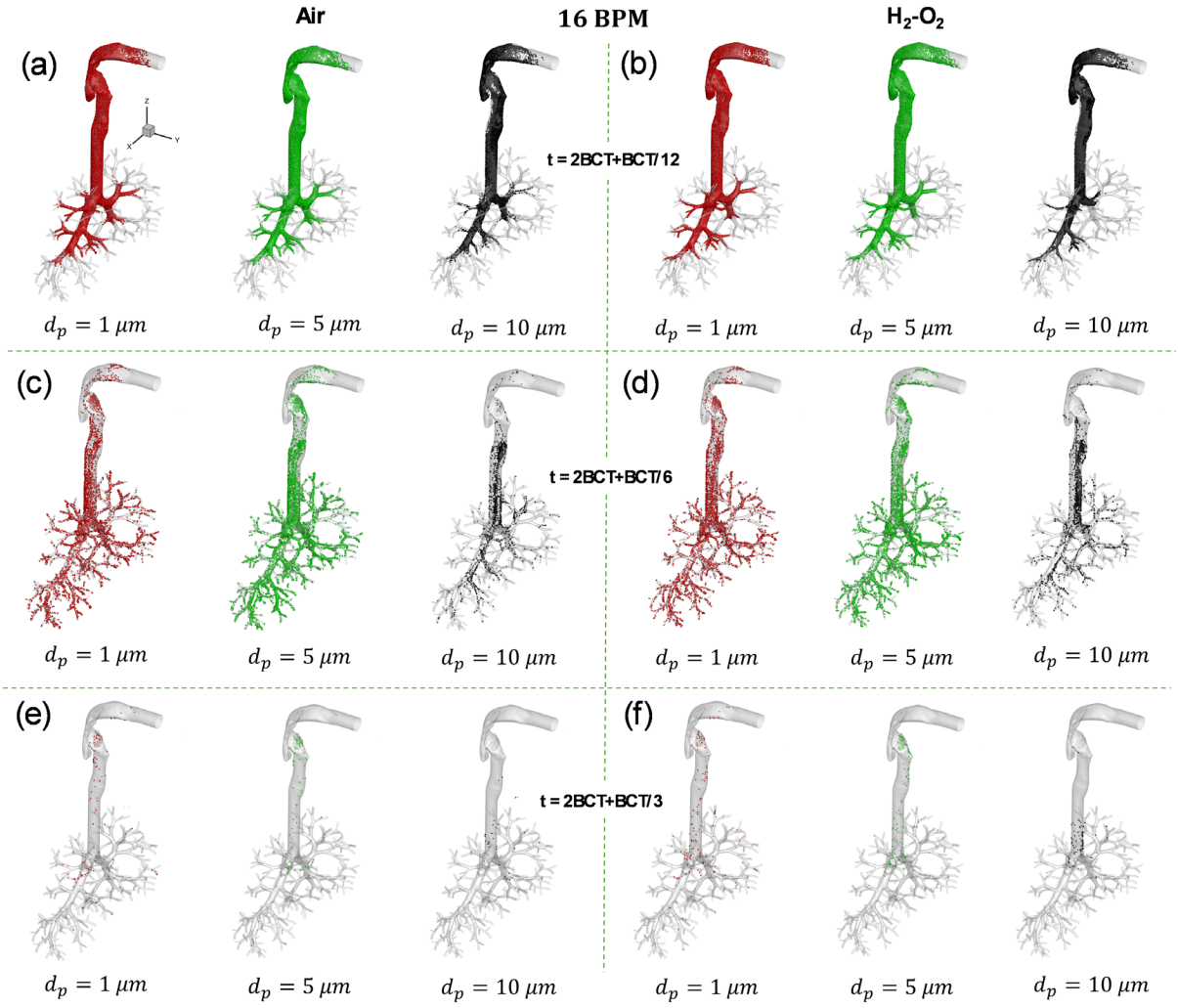

FIG. 15. Distributions of suspending particles at multiple time stations with BPM = 16: (a) t = 2BCT + BCT/12 with air, (b) t = 2BCT + BCT/12 with H_2–O_2 gas mixture, (c) t = 2BCT + BCT/6 with air, (d) t = 2BCT + BCT/6 with H_2–O_2 gas mixture, (e) t = 2BCT + BCT/3 with air, and (f) t = 2BCT + BCT/3 with H_2–O_2 gas mixture.

mixed with O_2, the extremely low density and high diffusivity of H_2 could theoretically increase the risk if it enters the vasculature directly (e.g., through a traumatic injury during ventilation). Its rapid diffusion could cause bubbles to form or expand, causing potential gas embolism. In addition, it could introduce anti-inflammatory and anti-apoptotic signaling due to biological activity such as modulating various cell signaling pathways (Ohta, 2015). The systemic impact of this when used as a routine carrier gas is completely unknown and could interfere with the intended action of the inhaled drug or the patient's baseline physiology. Furthermore, inhaling low density could cause voice and sensory alterations. Although there is no direct evidence to prove such issues caused by H_2, the clinically used low-density gas (i.e., Heliox) explicitly mentions the "Donald Duck" voice alteration as a common and expected side effect (Hess and Chatmongkolchart, 2000; Slinger *et al.*, 2019), implying this could also happen in other low-density gas environments such as H_2–O_2 gas mixture. However, more evidence upon the potential physiological effects of H_2–O_2 gas mixture is still needed to help inhalation therapy research community better understand the potential risks in lab or in clinic.

IV. CONCLUSIONS

Employing an experimentally validated CFPD model, this study investigated how replacing conventional air with the H_2–O_2 gas mixture in a 2:1 volumetric ratio as the inhaled medicinal particle carrier influences pulmonary gas-particle transport and deposition in a representative human respiratory system, specifically focusing on the potential enhancement of delivered dose to the peripheral lung (i.e., G13-to-alveoli regions). Various breathing patterns (12, 16, and 20 BPM) and particle sizes (1, 5, and 10 μm) were analyzed to evaluate their combined effects on flow behavior, turbulence characteristics, and particle deposition efficiency. The key conclusions are summarized as follows:

(1) Compared with air, the H_2–O_2 gas mixture generated lower WSS, and a pressure drop from the mouth to G13. This

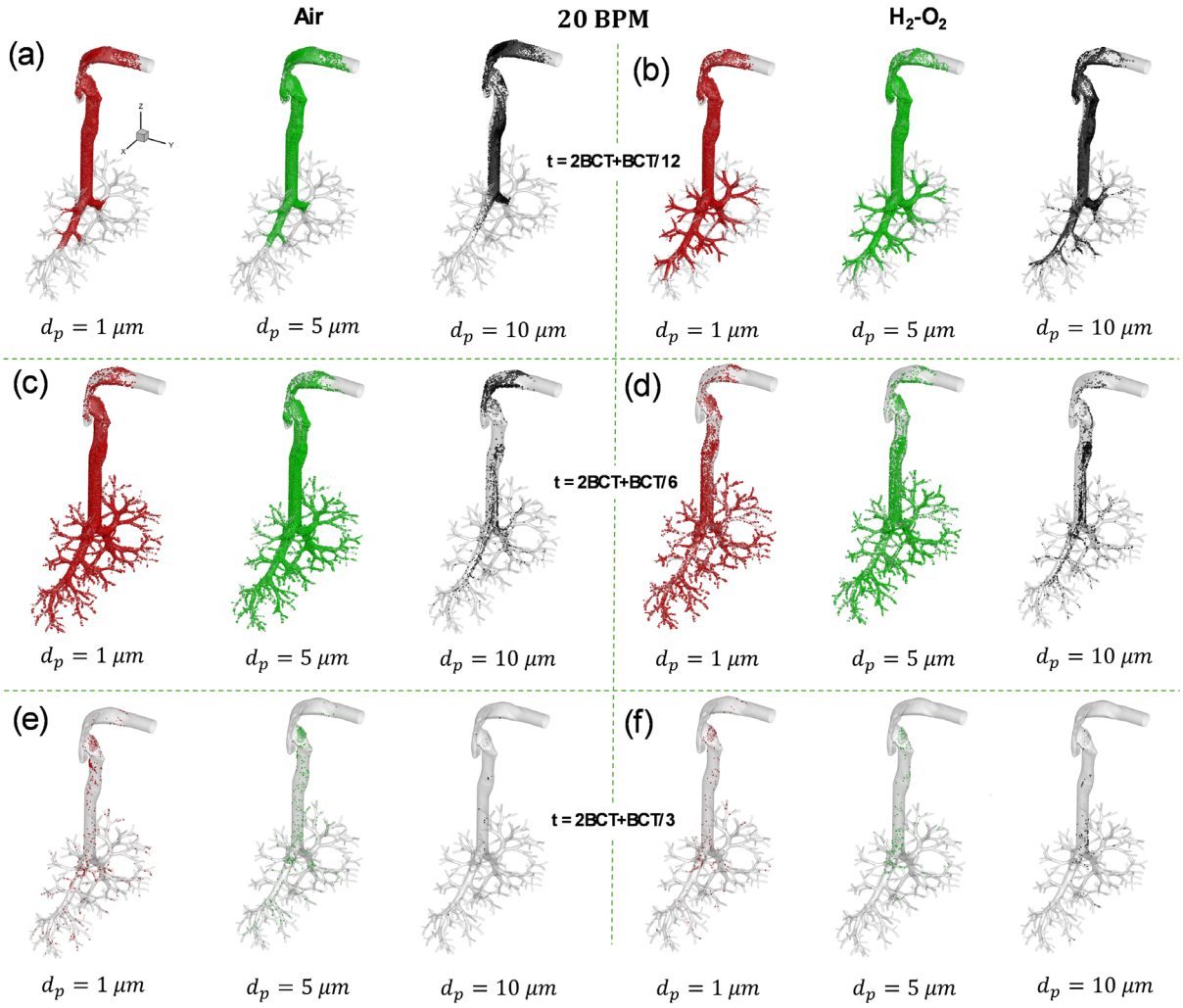

FIG. 16. Distributions of suspending particles at multiple time stations with BPM = 20: (a) t = 2BCT + BCT/12 with air, (b) t = 2BCT + BCT/12 with H_2–O_2 gas mixture, (c) t = 2BCT + BCT/6 with air, (d) t = 2BCT + BCT/6 with H_2–O_2 gas mixture, (e) t = 2BCT + BCT/3 with air, and (f) t = 2BCT + BCT/3 with H_2–O_2 gas mixture.

indicates that the H_2–O_2 gas mixture can provide a milder mechanical environment within the human respiratory system, reducing the likelihood of airway irritation or epithelial injury during inhalation therapy.

(2) With higher kinematic viscosity compared with air, the H_2–O_2 gas mixture produced lower Reynolds numbers under equivalent breathing conditions. As a result, the mixture exhibited lower TKE and reduced inertial impaction and turbulence dispersion effect throughout the inhalation phase. These features interactively reduce particle deposition in the upper airway.

(3) Across all particle diameters and breathing patterns investigated in this study, the use of H_2–O_2 gas mixture led to lower RDFs from mouth to G13, thereby increasing particle transport to the G13-to-alveolar region. This improvement in distal deposition efficiency, up to 9.16%, was consistently observed across breathing conditions. These results confirm that reduced turbulence intensity and flow resistance achieved with the H_2–O_2 gas mixture facilitate deeper particle penetration into the pulmonary periphery.

(4) With the fixed tidal volume, increasing BPM enhanced inertial impaction and turbulence intensity, leading to higher deposition in the upper airway and lower delivery efficiency to the peripheral lung. Lower BPM allows more particles to reach deeper airway generations. These findings support the clinical recommendation that slower, deeper inhalation improves drug delivery efficiency to small airways.

(5) With the particle diameter increased from 1 to 10 μm, RDFs in the peripheral lung (i.e., G13-to-alveoli) decreased monotonically, while deposition in the upper and tracheobronchial regions increased due to enhanced inertial impaction and gravitational sedimentation. Larger particles exhibited lower aerodynamic responsiveness and longer relaxation times, causing them to deviate from streamlines and deposit preferentially in regions of high curvature or bifurcation, such as the oropharynx and

main bronchus. In contrast, smaller particles (<5 μm) followed airflow more closely and were more likely to reach distal airways.

(6) The highest deposition efficiency in the G13-to-alveoli region was achieved when 1 μm particles were inhaled at 12 BPM using the H_2–O_2 gas mixture as the carrier. This condition yielded the most favorable combination of reduced turbulence, minimal upper-airway deposition, and effective transport to the peripheral lung.

In summary, the use of H_2–O_2 gas mixture as an alternative carrier gas can potentially enhance targeted pulmonary drug delivery by reducing turbulence-induced particle loss in the upper airways and promoting deeper penetration into the lung. The findings highlight the combined importance of gas properties, particle size, and breathing pattern in optimizing inhalation therapy performance. Nevertheless, before clinical application, the potential physiological impacts of using the H_2–O_2 gas mixture, such as hyperoxia risks and altered gas exchange dynamics, must be thoroughly evaluated through *in vivo* or clinical investigations.

V. LIMITATIONS AND FUTURE WORK

The current study includes a few simplifications and assumptions listed below that may limit the generalization of the findings. Future work is also presented below to address each limitation of the current study.

(1) The CFPD simulations were limited to the respiratory system geometry from mouth to G13, with the downstream distal regions excluded from the computational domain. Accordingly, the outlet condition uses zero-gauge pressure at the G13 terminals as a pressure reference for the truncated domain. While this is a standard and well-posed approach for driving flow with a prescribed inlet waveform, it does not represent subject-specific distal lung mechanics (e.g., regional compliance/airway resistance, time-varying alveolar pressure, or asymmetric distal impedance). These omitted distal effects may influence local pressure levels and flow partitioning near terminal outlets. Future work will incorporate distal lung models (e.g., multiscale 3D–1D coupling) to represent downstream impedance and time-varying alveolar pressure more physiologically and to quantify the sensitivity of terminal flow split and deposition metrics to outlet modeling assumptions.

(2) The particle sizes investigated (i.e., 1, 5, and 10 μm) may not fully capture the complete size range of inhalable medicinal particulate matter. Moreover, particle size changes due to evaporation, condensation, or coalescence were not considered, which could alter the transport and deposition predictions, especially under humid airway conditions. Future work will incorporate dynamic droplet size evolution and humidity-dependent effects to represent real inhalation scenarios better.

(3) The current CFPD model assumes rigid airway wall boundary conditions and constant wall temperature, neglecting wall motion and heat/mass transfer between the gas and airway tissues. Subsequent research will extend the current CFPD modeling framework to include fluid–structure interaction (FSI) and transient thermal coupling for improved physiological accuracy.

(4) The study employed only one upper airway geometry (Chen *et al.*, 2024). Although previous work (Feng *et al.*, 2018) suggests consistent trends in regional deposition across individuals, anatomical variability in upper airway morphology can still meaningfully influence deposition patterns. To assess intersubject variability, we will construct a virtual cohort comprising multiple patient-specific upper airway geometries. This will allow systematic analysis of geometric variability on pulmonary gas-particle flow dynamics, delivered dose distribution, and the robustness of H_2–O_2 gas mixture-based inhalation therapy across diverse populations.

(5) This study was purely computational for testing the feasibility of such a prototype inhalation therapy methodology. Future efforts will focus on experimental validation using *in vitro* airway replicas and *in vivo* imaging data to verify the predicted flow fields and deposition patterns. Combining validated CFPD results with multiscale modeling and clinical measurements will further enhance confidence in the use of the H_2–O_2 gas mixture as a potential carrier for targeted pulmonary drug delivery.

SUPPLEMENTARY MATERIAL

See the supplementary material for the quantitative assessment of the Soret effect on pulmonary gas flow field prediction in this study.

ACKNOWLEDGMENTS

The authors acknowledge Dr. Ying Zheng (Department Head and Professor, Department of Pharmaceutical Sciences, University of Macau) for initially proposing the concept of using H_2–O_2 gas mixture as a carrier for inhalation therapy, which she claimed to be a world-first original idea. The use of Ansys software (Ansys, Inc., Canonsburg, PA) as part of the Ansys-CBBL academic partnership is also gratefully acknowledged (Thierry Marchal and Vishal Ganore).

AUTHOR DECLARATIONS

Conflict of Interest

The authors have no conflicts to disclose.

Author Contributions

Hang Yi: Conceptualization (equal); Data curation (lead); Formal analysis (lead); Investigation (lead); Methodology (equal); Validation (lead); Visualization (lead); Writing – original draft (lead); Writing – review & editing (supporting). **Yu Feng:** Conceptualization (equal); Data curation (supporting); Formal analysis (supporting); Investigation (supporting); Methodology (equal); Project administration (lead); Resources (lead); Software (lead); Supervision (lead); Validation (supporting); Visualization (supporting); Writing – original draft (supporting); Writing – review & editing (lead).

DATA AVAILABILITY

The data that support the findings of this study are available from the corresponding author upon reasonable request.

REFERENCES

Abdo, W. F. and Heunks, L. M., "Oxygen-induced hypercapnia in COPD: Myths and facts," Crit. Care **16**(5), 323 (2012).

Ainetdinov, R. M., Antonov, D. V., Avdeev, S. N., Cao, B. Y., Kerimbekova, S. A., Liu, N., Merzhoeva, Z. M., Nagatkina, O. V., Nikitina, L. Y., Rybdylova, O., Sazhin, S. S., Sokolova, E. S., Strizhak, P. A., and Suvorova, O. A., "Achievements and challenges of targeted drug delivery to a human respiratory tract: Bridging traditional and novel approaches to modelling and clinical needs," J. Aerosol Sci. **191**, 106706 (2026).

Allen, M. D. and Raabe, O. G., "Slip correction measurements of spherical solid aerosol particles in an improved Millikan apparatus," Aerosol Sci. Technol. **4**(3), 269–286 (1985).

Banko, A. J., Coletti, F., Elkins, C. J., and Eaton, J. K., "Oscillatory flow in the human airways from the mouth through several bronchial generations," Int. J. Heat Fluid Flow **61**, 45–57 (2016).

Bardsley, G., Pilcher, J., McKinstry, S., Shirtcliffe, P., Berry, J., Fingleton, J., Weatherall, M., and Beasley, R., "Oxygen versus air-driven nebulisers for exacerbations of chronic obstructive pulmonary disease: A randomised controlled trial," BMC Pulm. Med. **18**(1), 157 (2018).

Benra, F.-K., Dohmen, H., Pei, J., Schuster, S., and Wan, B., "A comparison of one-way and two-way coupling methods for numerical analysis of fluid-structure interactions," J. Appl. Math. **2011**, 853560.

Borghardt, J. M., Kloft, C., and Sharma, A., "Inhaled therapy in respiratory disease: The complex interplay of pulmonary kinetic processes," Can. Respir. J. **2018**(1), 2732017.

Borgström, L., Olsson, B., and Thorsson, L., "Degree of throat deposition can explain the variability in lung deposition of inhaled drugs," J. Aerosol. Med. **19**(4), 473–483 (2006).

Brubakk, A. O., Neuman, T. S., and Elliott, D. H., *Bennett and Elliott's Physiology and Medicine of Diving* (Saunders, 2003).

Bui, V. K. H., Moon, J.-Y., Chae, M., Park, D., and Lee, Y.-C., "Prediction of aerosol deposition in the human respiratory tract via computational models: A review with recent updates," Atmosphere **11**(2), 137 (2020).

Chen, H., Harui, A., Feng, Y., Li, L., Patel, S., Schmidt, J., Roth, M. D., and Zhu, Y., "A ventilated three-dimensional artificial lung system for human inhalation exposure studies," Environ. Sci. Technol. **58**(52), 22919–22929 (2024).

Chen, X., Feng, Y., Zhong, W., and Kleinstreuer, C., "Numerical investigation of the interaction, transport and deposition of multicomponent droplets in a simple mouth-throat model," J. Aerosol Sci. **105**, 108–127 (2017).

Chen, X., Feng, Y., Zhong, W., Sun, B., and Tao, F., "Numerical investigation of particle deposition in a triple bifurcation airway due to gravitational sedimentation and inertial impaction," Powder Technol. **323**, 284–293 (2018).

Cole, A. R., Sperotto, F., DiNardo, J. A., Carlisle, S., Rivkin, M. J., Sleeper, L. A., and Kheir, J. N., "Safety of prolonged inhalation of hydrogen gas in air in healthy adults," Crit. Care Explor. **3**(10), e543 (2021).

Derjaguin, B. V., Rabinovich, Y. I., Storozhilova, A. I., and Shcherbina, G. I., "Measurement of the coefficient of thermal slip of gases and the thermophoreses velocity of large-size aerosol particles," J. Colloid Interface Sci. **57**(3), 451–461 (1976).

Farooq, U., Riaz, H. H., Munir, A., Tariq, A., Chan, T. C., Zhao, M., and Islam, M. S., "Heliox: An advanced method for targeted drug delivery in respiratory airways," J. Taiwan Inst. Chem. Eng. **176**, 106323 (2025).

Farooq, U., Riaz, H. H., Munir, A., Zhao, M., Tariq, A., and Islam, M. S., "Application of heliox for optimized drug delivery through respiratory tract," Phys. Fluids **35**(10), 103321 (2023).

Feng, Y., Kleinstreuer, C., Castro, N., and Rostami, A., "Computational transport, phase change and deposition analysis of inhaled multicomponent droplet–vapor mixtures in an idealized human upper lung model," J. Aerosol Sci. **96**, 96–123 (2016).

Feng, Y., Kleinstreuer, C., and Rostami, A., "Evaporation and condensation of multicomponent electronic cigarette droplets and conventional cigarette smoke particles in an idealized G3–G6 triple bifurcating unit," J. Aerosol Sci. **80**, 58–74 (2015).

Feng, Y., Zhao, J., Chen, X., and Lin, J., "An in silico subject-variability study of upper airway morphological influence on the airflow regime in a tracheobronchial tree," Bioengineering **4**(4), 90 (2017).

Feng, Y., Zhao, J., Hayati, H., Sperry, T., and Yi, H., "Tutorial: Understanding the transport, deposition, and translocation of particles in human respiratory systems using computational fluid-particle dynamics and physiologically based toxicokinetic models," J. Aerosol Sci. **151**, 105672 (2021).

Feng, Y., Zhao, J., Kleinstreuer, C., Wang, Q., Wang, J., Wu, D. H., and Lin, J., "An in silico inter-subject variability study of extra-thoracic morphology effects on inhaled particle transport and deposition," J. Aerosol Sci. **123**, 185–207 (2018).

Foncerrada, G., Culnan, D. M., Capek, K. D., González-Trejo, S., Cambiaso-Daniel, J., Woodson, L. C., Herndon, D. N., Finnerty, C. C., and Lee, J. O., "Inhalation injury in the burned patient," Ann. Plast. Surg. **80**(3), S98–S105 (2018).

Fung, W. Y. and Siu, M. T., "Optimizing the effectiveness of inhalation therapy-comprehensive knowledge enhancement program," Eur. Respir. J. **54**(suppl 63), PA4195 (2019).

Guan, W.-J., Wei, C.-H., Chen, A.-L., Sun, X.-C., Guo, G.-Y., Zou, X., Shi, J.-D., Lai, P.-Z., Zheng, Z.-G., and Zhong, N.-S., "Hydrogen/oxygen mixed gas inhalation improves disease severity and dyspnea in patients with Coronavirus disease 2019 in a recent multicenter, open-label clinical trial," J. Thorac. Dis. **12**(6), 3448–3452 (2020).

Haghnegahdar, A., Zhao, J., and Feng, Y., "Lung aerosol dynamics of airborne influenza A virus-laden droplets and the resultant immune system responses: An in silico study," J. Aerosol Sci. **134**, 34 (2019).

Hagmeyer, L., van Koningsbruggen-Rietschel, S., Matthes, S., Rietschel, E., and Randerath, W., "From the infant to the geriatric patient—Strategies for inhalation therapy in asthma and chronic obstructive pulmonary disease," Clin. Respir. J. **17**(6), 487–498 (2023).

Hess, D. and Chatmongkolchart, S., "Techniques to avoid intubation: Noninvasive positive pressure ventilation and heliox therapy," Int. Anesthesiol. Clin. **38**(3), 161–187 (2000).

Heyder, J., Gebhart, J., Rudolf, G., Schiller, C. F., and Stahlhofen, W., "Deposition of particles in the human respiratory tract in the size range 0.005–15 μm," J. Aerosol Sci. **17**(5), 811–825 (1986).

Hofmann, W., "Modelling inhaled particle deposition in the human lung—A review," J. Aerosol Sci. **42**(10), 693–724 (2011).

Islam, M. S., Gu, Y., Farkas, A., Paul, G., and Saha, S. C., "Helium–oxygen mixture model for particle transport in CT-based upper airways," Int. J. Environ. Res. Public Health **17**(10), 3574 (2020).

Jin, J., Yue, L., Du, M., Geng, F., Gao, X., Zhou, Y., Lu, Q., and Pan, X., "Molecular hydrogen therapy: Mechanisms, delivery methods, preventive, and therapeutic application," MedComm **6**(5), e70194 (2025).

Johnsen, H. M., Hiorth, M., and Klaveness, J., "Molecular hydrogen therapy—A review on clinical studies and outcomes," Molecules **28**(23), 7785 (2023).

Kitaoka, H., Koc, S., Tetsumoto, S., Koumo, S., Hirata, H., and Kijima, T., "4D model generator of the human lung, "Lung4Cer"," in *Annual International Conference of the IEEE Engineering in Medicine and Biology Society* (IEEE, 2013), pp. 453–456.

Kleinstreuer, C. and Zhang, Z., "Airflow and particle transport in the human respiratory system," Annu. Rev. Fluid Mech. **42**(1), 301–334 (2010).

Kuprat, A. P., Feng, Y., Corley, R. A., and Darquenne, C., "Subject-specific multiscale modeling of the fate of inhaled aerosols," J. Aerosol Sci. **183**, 106471 (2025).

Li, A. and Ahmadi, G., "Dispersion and deposition of spherical particles from point sources in a turbulent channel flow," Aerosol Sci. Technol. **16**(4), 209–226 (1992).

Liu, C., Tian, X., Wang, Z., Mak, J. C. W., Mao, S., Liu, T.-M., and Zheng, Y., "Hydrogen-induced disruption of the airway mucus barrier enhances nebulized RNA delivery to reverse pulmonary fibrosis," Sci. Adv. **11**(16), eadt2752 (2025).

Liu, Y., Chen, X., Xie, J., Xie, X., Zhang, Y., and Tao, F., "Numerical simulation of high-concentration droplet flow in an idealized mouth–throat airway model in the influence of environmental temperature and humidity," Phys. Fluids **36**(12), 123361 (2024).

Longest, P. W., Bass, K., Dutta, R., Rani, V., Thomas, M. L., El-Achwah, A., and Hindle, M., "Use of computational fluid dynamics deposition modeling in respiratory drug delivery," Expert Opin. Drug Delivery **16**(1), 7–26 (2019).

Lukerchenko, N., Kvurt, Y., Keita, I., Chara, Z., and Vlasak, P., "Drag force, drag torque, and magnus force coefficients of rotating spherical particle moving in fluid," Part. Sci. Technol. **30**(1), 55–67 (2012).

Mach, W. J., Thimmesch, A. R., Pierce, J. T., and Pierce, J. D., "Consequences of hyperoxia and the toxicity of oxygen in the lung," Nurs. Res. Pract. **2011**, 260482.

Mason, E. A. and Chapman, S., "Motion of small suspended particles in nonuniform gases," J. Chem. Phys. **36**(3), 627–632 (1962).
Menter, F. R., Langtry, R., and Völker, S., "Transition modelling for general purpose CFD codes," Flow, Turbul. Combust. **77**, 277–303 (2006).
Morsi, S. and Alexander, A., "An investigation of particle trajectories in two-phase flow systems," J. Fluid Mech. **55**(2), 193–208 (1972).
Newman, S. P., Agnew, J. E., Pavia, D., and Clarke, S. W., "Inhaled aerosols: Lung deposition and clinical applications," Clin. Phys. Physiol. Meas. **3**(1), 1 (1982).
Nof, E., Heller-Algazi, M., Coletti, F., Waisman, D., and Sznitman, J., "Ventilation-induced jet suggests biotrauma in reconstructed airways of the intubated neonate," J. R. Soc. Interface **17**(162), 20190516 (2020).
Ohta, S., "Molecular hydrogen as a preventive and therapeutic medical gas: Initiation, development and potential of hydrogen medicine," Pharmacol. Ther. **144**(1), 1–11 (2014).
Ohta, S., "Molecular hydrogen as a novel antioxidant: Overview of the advantages of hydrogen for medical applications," Methods Enzymol. **555**, 289–317 (2015).
Reper, P. and Heijmans, W., "High-frequency percussive ventilation and initial biomarker levels of lung injury in patients with minor burns after smoke inhalation injury," Burns **41**(1), 65–70 (2015).
Rocourt, X., Mélani, L., Sochet, I., and Jallais, S., "Flammability limits of hydrogen mixtures diffusing in air," in 31st Meeting on Combustion of the Italian Section of the Combustion Institute (2008).
Saha, S. C. and Islam, M. S., "Airflow and particle transport to the terminal bronchioles during heliox breathing," in Proceedings of 16th Asian Congress of Fluid Mechanics (2021).
Scichilone, N., "Asthma control: The right inhaler for the right patient," Adv. Ther. **32**(4), 285–292 (2015).
Shi, M.-M., Chen, Y.-T., Wang, X.-D., Zhang, Y.-F., Cheng, T., Chen, H., Sun, F., Bao, H., Chen, R., Xiong, W.-N., Song, Y.-L., Li, Q.-Y., and Qu, J.-M., "The efficacy of hydrogen/oxygen therapy favored the recovery of omicron SARS-CoV-2 variant infection: Results of a multicenter, randomized, controlled trial," J. Clin. Biochem. Nutr. **73**(3), 228–233 (2023).
Slinger, C., Slinger, R., Vyas, A., Haines, J., and Fowler, S. J., "Heliox for inducible laryngeal obstruction (vocal cord dysfunction): A systematic literature review," Laryngoscope Invest. Otolaryngol. **4**(2), 255–258 (2019).
Steiropoulos, P., Bakakos, P., Hatziagorou, E., Katsaounou, P., Loukides, S., Papaioannou, A. I., Porpodis, K., Samaras, K., Tzouvelekis, A., Kalafatakis, K., and Kostikas, K., "The present and future of inhalation therapy for the management of obstructive airway diseases: Emphasis on pressurized metered-dose inhalers," Pneumon **34**(4), 24 (2021).
Takemura, M., Mitsui, K., Itotani, R., Ishitoko, M., Suzuki, S., Matsumoto, M., Aihara, K., Oguma, T., Ueda, T., Kagioka, H., and Fukui, M., "Relationships between repeated instruction on inhalation therapy, medication adherence, and health status in chronic obstructive pulmonary disease," Int. J. Chronic Obstruct. Pulm. Dis. **6**, 97–104 (2011).
Talbot, L., Cheng, R. K., Schefer, R. W., and Willis, D. R., "Thermophoresis of particles in a heated boundary layer," J. Fluid Mech. **101**(4), 737–758 (1980).
Tian, L. and Ahmadi, G., "Computational modeling of fiber transport in human respiratory airways—A review," Exp. Comput. Multiphase Flow **3**(1), 1–20 (2021).
Usmani, O. S., Biddiscombe, M. F., and Barnes, P. J., "Regional lung deposition and bronchodilator response as a function of beta2-agonist particle size," Am. J. Respir. Crit. Care Med. **172**(12), 1497–1504 (2005).
van der Zwaan, I., Pilkington, G. A., Frenning, G., Ekström, M., Valetti, S., Pitcairn, G. R., and Feiler, A., "Influence of particle diameter on aerosolization performance and release of budesonide loaded mesoporous silica particles," Eur. J. Pharm. Sci. **200**, 106828 (2024).
Walker, K. L., Geyling, F. T., and Nage, S. R., "Thermophoretic deposition of small particles in the modified chemical vapor deposition (MCVD) process," J. Am. Ceram. Soc. **63**(9–10), 552–558 (1980).
Wang, S., Bao, C., He, Y., Tian, X., Yang, Y., Zhang, T., and Xu, K., "Hydrogen gas (XEN) inhalation ameliorates airway inflammation in asthma and COPD patients," QJM: An Int. J. Med. **113**(12), 870–875 (2020).
Woodward, I. R. and Fromen, C. A., "Recent developments in aerosol pulmonary drug delivery: New technologies, new cargos, and New targets," Annu. Rev. Biomed. Eng. **26**, 307–330 (2024).
Zajac, D., Jampolska, M., and Wojciechowski, P., "Molecular hydrogen in the treatment of respiratory diseases," Int. J. Mol. Sci. **26**(9), 4116 (2025).
Zhang, N., Deng, C., Zhang, X., Zhang, J., and Bai, C., "Inhalation of hydrogen gas attenuates airway inflammation and oxidative stress in allergic asthmatic mice," Asthma Res. Pract. **4**(1), 3 (2018).
Zhang, Z. and Kleinstreuer, C., "Laminar-to-turbulent fluid–nanoparticle dynamics simulations: Model comparisons and nanoparticle-deposition applications," Int. J. Numer. Methods Biomed. Eng. **27**(12), 1930–1950 (2011).
Zhang, Z., Kleinstreuer, C., and Hyun, S., "Size-change and deposition of conventional and composite cigarette smoke particles during inhalation in a subject-specific airway model," J. Aerosol Sci **46**, 34–52 (2012).
Zhao, J., Feng, Y., Koshiyama, K., and Wu, H., "Prediction of airway deformation effect on pulmonary air-particle dynamics: A numerical study," Phys. Fluids **33**(10), 101906 (2021).
Zheng, Z.-G., Sun, W.-Z., Hu, J.-Y., Jie, Z.-J., Xu, J.-F., Cao, J., Song, Y.-L., Wang, C.-H., Wang, J., Zhao, H., Guo, Z.-L., and Zhong, N.-S., "Hydrogen/oxygen therapy for the treatment of an acute exacerbation of chronic obstructive pulmonary disease: Results of a multicenter, randomized, double-blind, parallel-group controlled trial," Respir. Res. **22**(1), 149 (2021).
Zhou, Z. Q., Zhong, C. H., Su, Z. Q., Li, X. Y., Chen, Y., Chen, X. B., Tang, C. L., Zhou, L. Q., and Li, S. Y., "Breathing hydrogen-oxygen mixture decreases inspiratory effort in patients with tracheal stenosis," Respiration **97**(1), 42–51 (2019).